

Energy & Environmental Science

Accepted Manuscript



This is an *Accepted Manuscript*, which has been through the Royal Society of Chemistry peer review process and has been accepted for publication.

Accepted Manuscripts are published online shortly after acceptance, before technical editing, formatting and proof reading. Using this free service, authors can make their results available to the community, in citable form, before we publish the edited article. We will replace this *Accepted Manuscript* with the edited and formatted *Advance Article* as soon as it is available.

You can find more information about *Accepted Manuscripts* in the [Information for Authors](#).

Please note that technical editing may introduce minor changes to the text and/or graphics, which may alter content. The journal's standard [Terms & Conditions](#) and the [Ethical guidelines](#) still apply. In no event shall the Royal Society of Chemistry be held responsible for any errors or omissions in this *Accepted Manuscript* or any consequences arising from the use of any information it contains.

BiCuSeO oxyselenides: new promising thermoelectric materials

Li-Dong Zhao,^{*a} Jiaqing He,^b David Berardan,^a Yuanhua Lin,^c Jing-Feng Li,^c Ce-Wen Nan,^c Nita Dragoë^{*a}

^a*SP2M, ICMMO (CNRS UMR 8182), University Paris-Sud, Orsay F-91405, France
(Li-Dong Zhao is presently in Department of Chemistry, Northwestern University,
Evanston, IL 60208, USA.)*

^b*Department of Physics, South University of Science and Technology of China,
Shenzhen 518055, China*

^c*State Key Laboratory of New Ceramics and Fine Processing, School of Materials
Science and Engineering, Tsinghua University, Beijing 100084, China*

Corresponding authors: lidong-zhao@northwestern.edu, nita.dragoe@u-psud.fr

Abstract

BiCuSeO oxyselenides have recently acquired ever-increasing attentions and have been extensively studied as very promising thermoelectric materials. The ZT of BiCuSeO system was significantly increased from 0.5 to 1.4 in the past three years, which indicates that BiCuSeO oxyselenides are robust candidates for energy conversion applications. In this review, we first discuss and summarize the crystal structures, microstructures, electronic structures and physical/chemical properties of BiCuSeO oxyselenides. Then, the approaches successfully enhanced the thermoelectric performances in BiCuSeO system are outlined, which include increasing carriers concentration, optimizing Cu vacancies, simple and facile ball milling method, multifunctional Pb doping, band gap tuning, and increasing carrier mobility through texturing. Theoretical calculations to predict a maximum ZT in the BiCuSeO system are also described. Finally, a discussion of future possible strategies is proposed to aim at further enhancing the thermoelectric figure of merit of these materials.

Introduction

Providing a sustainable energy supply is becoming a major societal problem as fossil fuel supplies decrease while demand increases. Hence, the past few years have witnessed a surge in interest in developing alternative renewable energy technologies. In particular, thermoelectric materials have drawn vast attentions because thermoelectric effects enable direct conversion between thermal and electrical energy, and provide an alternative for power generation and refrigeration. The key parameter that defines the efficiency of thermoelectric materials is the ‘dimensionless figure of merit’ ZT which derives from a combination of three physical properties: thermal conductivity (κ), electrical conductivity (σ) and Seebeck coefficient (S), $ZT = (S^2\sigma/\kappa)T$, with the temperature T . The quantity of $S^2\sigma$ is defined as the power factor. Ideally, both electrical conductivity σ and Seebeck coefficient S must be large, while the thermal conductivity κ must be minimized. However, the well-known complex relationship among the three parameters makes it challenging to develop effective approaches to improve a overall ZT .

Since Seebeck observed thermoelectric phenomena in 1821 for the first time, thermoelectric materials have been developed for nearly 200 years. Historically, the development of thermoelectric materials can be divided into three generations.¹ From 1821 to 1950s-1960s for the first functioning devices fabricated, ZT is about 1.0, and the devices can operate at ~4-5% conversion efficiency; The second period extends to 1990s, during which period the new theoretical ideas relating to “size effects” and the search for new materials following the PGEC (phonon-glass electron-crystal) concept² stimulated new experimental research that eventually led to significant advances, resulting in ZT of 1.3-1.7. These second generation materials are expected to produce power generation devices with conversion efficiencies of 11-15%; The third generation of bulk thermoelectrics has been under development recently, new concepts and new technologies have pushed ZT to range from 1.8 to 2.2, and the predicted device conversion efficiency increased to ~15-20%, but no experimental evidence of such a large conversion efficiency in modules or of its stability upon time has been reported

yet.

The widely used approaches to enhance ZT can be summarized as: modifying the band structure,^{3,4} bands convergence,^{5,6} quantum confinement effects,⁷ electron energy barrier filtering to enhance Seebeck coefficients,⁸ nanostructuring,⁹⁻¹⁵ all-scale hierarchical architecturing^{16,17} to reduce lattice thermal conductivity, and band energy alignment between nano-precipitate/matrix to maintain carrier mobility.^{18,19} Most of these approaches aim to maintain a high power factor and/or reduce the lattice thermal conductivity. Alternatively, one can seek high performance in pristine thermoelectric materials with intrinsically low thermal conductivity,²⁰ which may arise from a large anharmonicity,²⁰⁻²² a large molecular weight,²³ a complex crystal structure,²⁴ charge density wave distortions,²⁵ and improve their electrical transport properties by optimizing the charge carriers concentration or tuning the band-gaps, *etc.*²⁶⁻³¹

According to the optimal working temperature, the thermoelectric materials can be divided into three applied temperature ranges.^{12, 14, 32} At low temperature ranges (200 K ~ 400 K), typical materials are bismuth chalcogenides (Bi-Sb-Te, Bi-Te-Se, and Bi-S),³³⁻³⁸ for middle temperature ranges (600 K ~ 900 K), typical materials are lead chalcogenides (PbTe, PbSe, and PbS),^{3, 5, 9, 16, 18, 39-42} magnesium group IV compounds (Mg-Si-Sn),^{6, 43, 44} Skutterudites,^{10, 45-50} half-Heusler alloys⁵¹⁻⁵⁵ and Clathrates,⁵⁶⁻⁵⁹ while in high temperature ranges (> 900 K), typical materials are silicon-germanium⁶⁰⁻⁶² and Zintl phases.^{23, 63-65} Most of the above thermoelectric materials are heavy-metal-based alloys, including earth-rare and cost elements. In addition, all above mentioned materials may not be attractive in practical applications, particularly when operating at high temperature, because their constituents can decompose, be oxidized, vaporize, or melt at high temperatures. Therefore, new potential thermoelectric materials, composed of nontoxic, earth-abundant, light, and cheap elements, are expected to play a vital role in extensive thermoelectric applications for energy conversion, examples are such as SrTiO₃, Sodium Cobalt, Calcium Cobalt, *etc.*⁶⁶

Since BiCuSeO oxyselenides have been reported as potential thermoelectric materials in 2010, they have attracted ever-increasing attentions and extensively

studied.³⁰ In this review, we summarize and discuss the crystal structures, microstructures, electronic structures and physical/chemical properties of BiCuSeO oxyselenides. The effective approaches that successfully enhanced the thermoelectric performance in BiCuSeO systems were summarized, specifically, increasing carriers concentration, optimizing Cu vacancies, simple and facile ball milling method, multifunctional Pb doping, band gap tuning, and increasing carrier mobility *via* texturing. A discussion of future possible strategies is aimed at enhancing the thermoelectric figure of merit of these materials.

1. A short review for conventional thermoelectric materials and BiCuSeO

As shown in **Fig. 1(a)**, the publications on BiCuSeO oxyselenides show an increasing trend since they have been reported as promising thermoelectric materials in 2010.³⁰ The research works involve many world leading groups in thermoelectric community. Many publications concerning the development of BiCuSeO oxyselenides appeared in the past three years, indicating indisputable interests on this system as the most promising candidate for the commercially thermoelectric application. It is interesting to compare BiCuSeO with the most advanced thermoelectric materials well known to date. **Fig. 1(b)** shows some typical state-of-the-art bulk thermoelectric materials developed in the last decades, which cover the temperature ranges from 200 K to 1200 K. In this plot, the conventional Bi₂Te₃-based (~300 K),³⁴ Pb(Ge)Te-based (~700 K)^{9, 16, 67} and SiGe-based (~1000 K)⁶⁰ alloys have been reinforced by advanced nanotechnology recently. At the beginning of 1990s, the search for new materials, such as Skutterudites⁶⁸ and Clathrates,⁵⁸ *etc*, was mainly motivated by the concept of Slack's "Phonon Glass-Electron Crystal".² In those compounds, the "rattling" motion of loosely bonded atoms within a large cage generates a strong phonon scattering but has less impact on the transport of carriers. Furthermore, Zintl phases with large and complex unit cells, including Yb₁₄MnSb₁₁,²³ Yb₁₁GaSb₉,⁶⁹ Ca₁₁GaSb₉⁷⁰ and SrZnSb₂⁷¹, have been revealed to possess intrinsically low lattice thermal conductivity due to the

high fraction of low velocity optical phonon modes, and the tremendous efforts were thereafter devoted to enhance the electrical transport properties of these Zintl phase materials. Alternatively, one can select compounds with promising electrical transport properties but relatively large lattice thermal conductivity, such as $\text{Mg}_2\text{Si-Mg}_2\text{Sn}$ ^{6, 44} and half-Heusler,^{51, 53-55, 72} *etc.* In these compounds, the reduction of the thermal conductivity would be very promising to enhance the thermoelectric figure of merit.

The ZT values of several materials, such as Bi_2Te_3 - and PbTe -based ones, well exceed unity and are sufficient for commercial applications but regardless of the environmental and materials cost. What's more, the emergence of some cutting-edge techniques and synergistic approaches make these bulk thermoelectric materials still lead the research frontier with record performances,¹ typical samples are nanostructured Bi-Sb-Te ,³⁴ $\text{AgPb}_m\text{SbTe}_{m+2}$ (LAST) with nano-dots,⁹ and hierarchical architecture PbTe-SrTe-Na ,¹⁶ *etc.* Although record ZT values realized, but there are very few reports about the thermoelectric modules performances yet, and their potential for real applications still need to be demonstrated. Apart from pursuing high record ZT , the new promising candidate is also very attractive. As shown in **Fig. 1(b)**, the maximum ZT of BiCuSeO exceeds 1 above 650K and monotonously increases up to 1.4 at 923K.⁷³ The average ZT , quantitatively represented by the area under the ZT vs. temperature curve, is the property that is being used extensively to estimate the performances in real application conditions. It can be seen that the average ZT of BiCuSeO outperforms several conventional thermoelectric materials. Moreover, compared with these conventional heavy-metal-based thermoelectric materials,^{12, 32} BiCuSeO oxyselenides consist of earth-abundant and non-toxic elements, and can thus be regarded as promising candidates for vehicle waste heat recovery and solar thermal engine replacement.

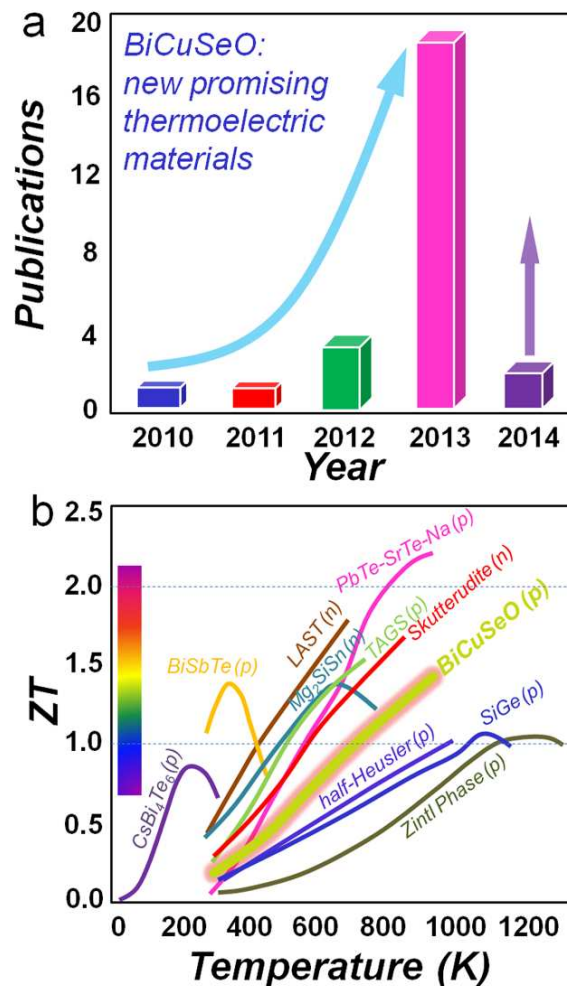


Fig. 1 (a) The number of publications on BiCuSeO oxyselenides as promising thermoelectric materials since 2010. (b) Dimensionless figure-of-merit ZT vs. temperature of typical current thermoelectric materials: CsBi₄Te₆,³³ Bi-Sb-Te,³⁴ AgPb_mSbTe_{m+2} (LAST),⁹ Mg₂SiSn,⁶ PbTe-SrTe-Na,¹⁶ Te-Ag-Ge-Sb (TAGS),⁶⁷ Skutterudite,⁴⁸ BiCuSeO,⁷³ half-Heusler,⁷² SiGe,⁶⁰ and Zintl phase.²³

2. Historical background and pristine features of BiCuSeO

In this section, firstly we introduce the history of BiCuSeO and its analogues, and then describe the features of pristine BiCuSeO including crystal structures, electronic structures, chemical and physical properties. For convenience, we summarized these parameters in **Table 1**.

Table 1. Crystallographic parameters, thermoelectric and elastic properties for BiCuSeO at room temperature.

Formula weight	367.4858
Crystal system	Tetragonal
Space group	<i>P4/nmm</i>
Unit cell dimensions	$a = 3.921 \text{ \AA}, \alpha = 90^\circ$
	$b = 3.921 \text{ \AA}, \beta = 90^\circ$
	$c = 8.913 \text{ \AA}, \gamma = 90^\circ$
Unit cell volume	137.06 \AA^3
<i>Z</i>	2
Theoretical density	8.9 g cm^{-3}
Carriers concentration	$1 \times 10^{18} \text{ cm}^{-3}$
Carriers mobility	$22 \text{ cm}^2 \text{ V}^{-1} \text{ s}^{-1}$
Band effective masses	Light hole band ($0.18 m_e$)
	Heavy hole band ($1.1 m_e$)
Seebeck coefficient	$349 \mu\text{VK}^{-1}$
Electrical conductivity	1.12 Scm^{-1}
Lattice thermal conductivity	$0.55 \text{ Wm}^{-1} \text{ K}^{-1}$
Longitudinal sound velocity	3290 ms^{-1}
Transverse sound velocity	1900 ms^{-1}
Average sound velocity	2107 ms^{-1}
Young's modulus	76.5 GPa
Debye temperature	243 K
Poisson ratio	0.25
Grüneisen parameter	1.5

Historical background:

The LaAgSO as an ancestry analogue of BiCuSeO, initially studied as an ionic conductor, was first reported by Palazzi *et al.* in 1980.⁷⁴ LaAgSO crystallizes in a layered ZrCuSiAs structure, with conductive AgS layers and charge reservoir LaO layers being mutually separated.⁷⁵ Due to the similarity of their layered crystal structure to that of cuprates, oxysulfides, or more generally oxychalcogenides, were thoroughly studied during the 1990s as new promising high temperature superconductors.⁷⁶⁻⁷⁸ Several isostructural compounds of general formula $RMChO$ ($R = \text{Bi or Ce to Dy}$, $M = \text{Cu or Ag}$, and $Ch = \text{S, Se or Te}$) were also discovered, they will be called “1111” in this article hereafter based on the stoichiometry.⁷⁹⁻⁸¹ However, no superconductivity was observed in any of these compounds, the interest in this family of materials gradually faded away. A few years later, apart from the superconductivity,

another interest in the 1111 oxychalcogenides was recurred because they might be promising in optoelectronic applications,⁸² since then, numerous 1111-type compounds have been synthesized.^{83, 84, 85}

The research on the superconductor in 1111-type compounds started a new era, which was ignited by the discovery of superconductivity in two new layered superconductors LaFePO⁸⁶ and LaNiPO⁸⁷ by Hosono *et al.* in 2006. Nevertheless, due to the very low critical temperature T_c , this discovery did not lead to enthusiastic reactions until 2008. Superconductivity with $T_c \sim 26$ K was observed by Hosono *et al.* in the F-doped LaFeAsO, which initiated a tremendous research toward the high T_c iron-based superconductors,⁸⁸ and T_c rapidly increased up to 43K^{89, 90} and 56 K.⁹¹ The discovery of superconductivity in the tetragonal iron-based pnictide has stimulated a tremendous search for superconductivity in a wide class of materials with similar structure. The effect of various substitutions on the low temperature properties of BiCuSeO system was investigated. Whatever the substitution (Bi substituted by Sr, Cu by Fe, Se by Te, and O by F), all samples revealed *p*-type, and no superconductivity was observed.⁹² Following this *Iron Rush era*, Dragoie *et al.* started to study the 1111 oxypnictides in 2008, just three months after $T_c \sim 26$ K reported, they found that LaFeAsO exhibits a large Seebeck coefficient peak and a promising power factor at around 100 K, which makes it promising for thermoelectric cooling applications in the cryogenic temperature range.^{93, 94} Dragoie *et al.* therefore decided to reevaluate the potential of the oxychalcogenides for thermoelectric applications. It was found that the thermoelectric figure-of-merit of these 1111-type oxychalcogenides are mainly restricted by their high electrical resistivity, which yet can be strongly reduced by tuning carriers concentration through routine doping.⁹⁵ Indeed, the Sr-doped BiCuSeO exhibits a promising ZT value of 0.76 at 873 K in 2010,³⁰ which was rapidly boosted to 1.4 at 923 K three years later,⁷³ as will be described hereafter. As of now BiCuSeO system has the highest reported ZT of all oxygen containing compounds exempt of Pb and Te, two elements that limit large scale applications owing to the high environmental and elements cost. It should be noted that the exp

Crystal structure:

BiCuSeO crystallizes in a layered ZrCuSiAs structure type,⁸¹ with the tetragonal unit cell $a = b = 3.9273 \text{ \AA}$, $c = 8.9293 \text{ \AA}$, $Z = 2$, and the space group $P4/nmm$ (No.129, PDF 45-0296), as listed in **Table 1**. **Fig. 2(a)** shows that, like every other $LnCuChO$ (Ln = lanthanide, Ch = S, Se, Te), BiCuSeO exhibits a two-dimensional (2D) layered structure containing fluorite like Bi_2O_2 layers alternatively stacked with Cu_2Se_2 layers along c -axis.^{96, 97} **Fig. 2(b)** shows the top-view along the c -axis. The Bi_2O_2 layers consist in slightly distorted Bi_4O tetrahedral, **Fig. 2(c)**, with two kinds of Bi-O-Bi bond angles, i.e., $\sim 106.95^\circ$ and $\sim 114.65^\circ$.^{80, 96-98} The coordination of Bi can also be considered as a distorted square antiprism with four O in one base and four Se in the other. The Bi-Se bond length $\sim 3.2 \text{ \AA}$ is longer than the Bi-O bond length $\sim 2.33 \text{ \AA}$, which implies its layered feature. The Cu_2Se_2 layers consist in slightly distorted $CuSe_4$ tetrahedral with Se-Se edges being shared, **Fig. 2(d)**. Two kinds of Se-Cu-Se bond angles exist, with the small one being $102.6^\circ \sim 106.95^\circ$ and the large one $113.1^\circ \sim 114.65^\circ$.^{80, 81, 95, 98} The Cu_2Se_2 layer could be considered as a reversed version of Bi_2O_2 layer, because the position of Se atoms is the same as that of Bi atoms, while the position of Cu atoms is the same as that of O atoms in Bi_2O_2 layer.^{80, 81, 95-98}

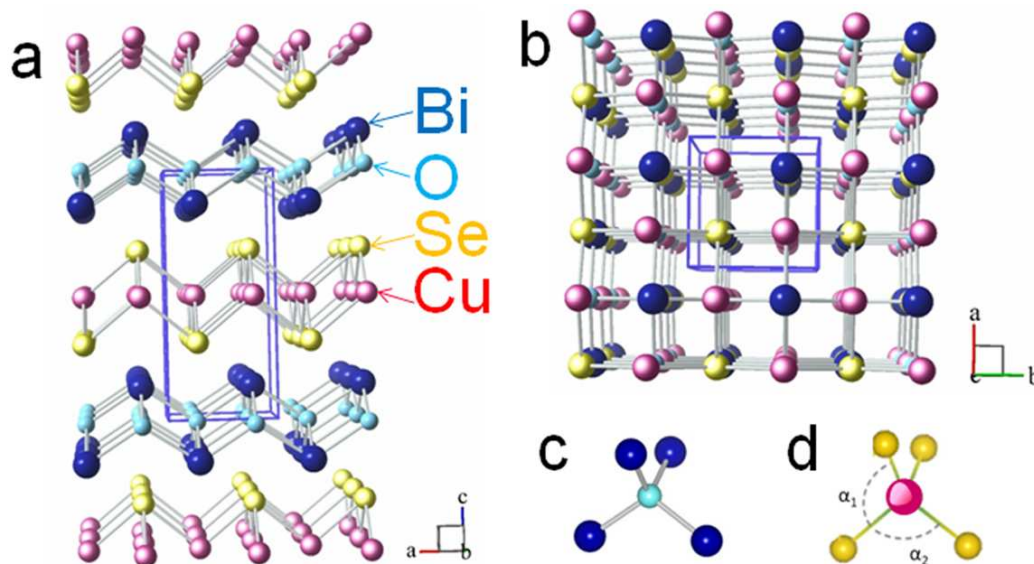


Fig. 2 (a) Crystal structure of BiCuSeO along b axis. (b) Structure along c axis. (c) Bi_4O tetrahedral. (d) $CuSe_4$ tetrahedral.

Electronic band structure and projected density-of-states (DOS):

Fig. 3 shows the electronic band structure and projected DOS of pristine BiCuSeO.⁹⁹ The main features are consistent with the results previously reported by Hiramatsu *et al.*⁹⁵ According to band structure calculation, BiCuSeO is a multiband material with an indirect band gap. From optical band gap measurements, the band gap is ~ 0.8 eV for bulk and powder, and ~ 1.0 eV for thin film. In BiCuChO, as Ch ions change from S to Se to Te, the band gap decreases from ~ 1.07 eV to 0.8 eV to 0.4 eV. The band gap of BiCuSeO is narrower than that of LaCuSeO (3.01 eV), mainly due to the low energy Bi 6*p* orbitals which are not present in LaCuSeO.⁹⁹ Bi 6*s* states are located deep in the valence band (-10 eV to -12 eV relative to the valence band maximum), as well as O 2*p* states (-5 eV to -7 eV).⁹⁹ The bottom of the conduction band mainly consists of Bi 6*p* states. The top of the valence band consists of bonding hybridized Cu 3*d*-Se 4*p* states nonbonding Cu 3*d* states (-1 eV to -3 eV) and antibonding hybridized Cu 3*d*-Se 4*p* states (close to the valence band maximum). It is noteworthy that in the vicinity of the Fermi level (0 eV to -0.5 eV) Cu and Se contribute almost equally to the DOS, with about 1 state eV⁻¹ fu⁻¹, and synergistically determine the electronic conduction.

As mention above, BiCuSeO is a multiband semiconductor.^{29, 99} The top of the valence band consists in a hole pocket located on the Γ -*M* line, **Fig. 3(b)**. Other hole pockets can be observed on the Γ -*X* line and at the *Z* point, which are located about -0.15 eV below the Fermi level, and participate the electronic conduction at high hole concentration or at high temperature. Surprisingly, a maximum located at the *Z* point for a 2D character of the crystal structure. Nevertheless, it is consistent with the projected DOS features as aforementioned. Therefore, it seems that although the electrical behavior of BiCuSeO will certainly be anisotropic, the anisotropy is probably moderate because of the moderate effective mass anisotropy, originating from the Bi 6*p* contribution to the DOS. The layered features of BiCuSeO structure motivate an expected strong anisotropy,^{100, 101} similarly to the artificial superlattices.¹⁰² However, both DOS calculations and transport measurements indicate that their electrical transport properties are closer to “classical 3D materials”, with almost parabolic-like dispersion relationship as compared to the 2D step-like DOS in superlattices.⁹⁹

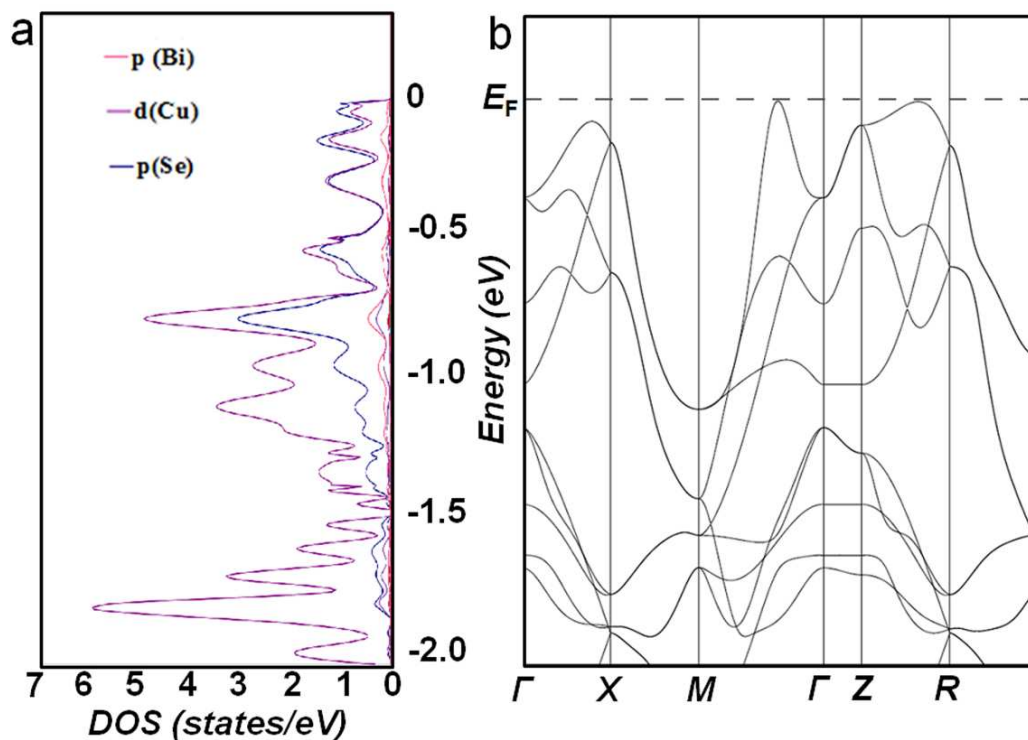


Fig. 3 (a) Electronic band structure. (b) Projected DOS for the undoped BiCuSeO. Reprinted (adapted) with permission from (ref 99). Copyright (2012) American Chemical Society.

Microstructures:

The layered structure of BiCuSeO has been investigated by advanced transmission electron microscopy (TEM),²⁹ the layered feature, i.e., conductive Cu-Se layers alternately stacked along the c axis with insulating Bi-O layers, can only be seen along non- c axes. As expected, lattice image along [001] zone axis (c axis) shows homogeneous contrast, **Fig. 4(a)**, and its fast Fourier transform image exhibits no spots splitting, **Fig. 4(d)**, both of which reveal that the two sublattices (Cu-Se and Bi-O) are commensurate along c axis. On the contrary, lattice images along [100] and [110] zone axes in **Fig. 4(b)** and **Fig. 4(c)** clearly show six-period (according to the stacking sequence -Bi-O-Bi-Se-Cu-Se-) layered structure, and the respective distinct spots splitting can be observed in fast Fourier transform images, as shown in **Fig. 4(f)** and **Fig. 4(h)**.²⁹

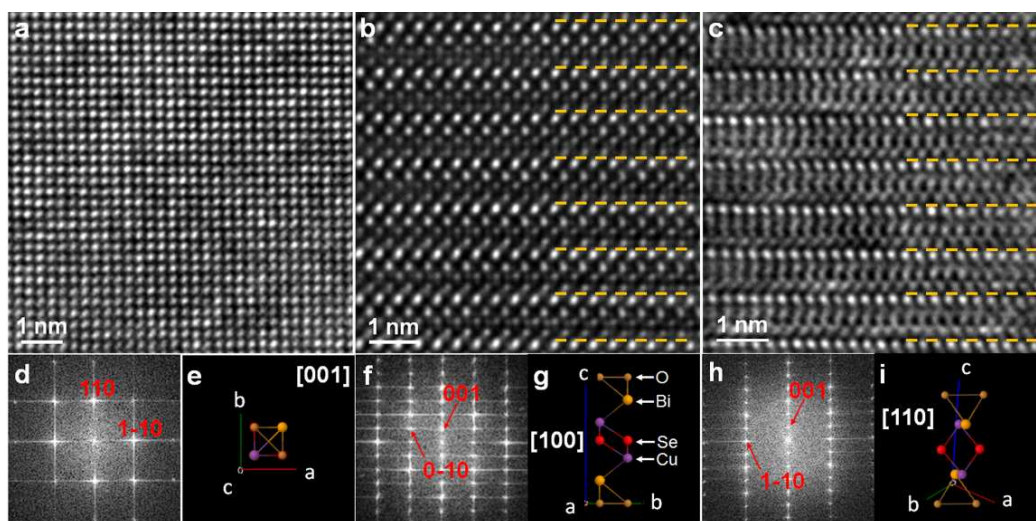


Fig. 4 HRTEM images of pristine BiCuSeO sample: (a), (b) and (c) Lattice images of along [001], [100] and [110] zone axes, respectively. (d), (f) and (h) Fast Fourier-transformed images of (a), (b) and (c), respectively. (e), (g) and (i) Crystal structures of BiCuSeO along [001], [100] and [110] zone axes, respectively.

A typical low-magnification TEM image shows lamellar grains with average width of 0.5 μm and length of 4 μm , **Fig. 5(a)**. The lamellar grains in mesoscale actually stem from the directional stacking of BiCuSeO layered lattices. Due to this lamellar microstructure, anisotropic transport properties can be expected in uniaxially densified pellets, as the density of grain boundaries will not be isotropic.²⁹ The TEM observations also reveal all types of relative orientations, i.e., coherent, semi-coherent and incoherent, between the lamellar grains. **Fig. 5(b)** shows a coherent boundary between two [001] direction grains, while a semi-coherent boundary also between two [001] direction grains but with $\sim 70^\circ$ rotation, as **Fig. 5(c)** shows. **Fig. 5(d)** is a typical high resolution TEM image of another boundary between two grains with a sharp and bright interface. The upper grain is along [100] direction while the direction of bottom grain is along [110]. Based on lattice image in **Fig. 5(d)**, the established atomic model, **Fig. 5(e)**, clearly shows the mismatch and misfit dislocations at the interface, which can also be seen from the real image in **Fig. 5(d)**. **Fig. 5(f)** and **Fig. 5(g)** are the fast Fourier transform images of **Fig. 5(d)** and **Fig. 5(e)**, revealing similar spot distribution. However, the fact that split spots along the c direction only present in **Fig. 5(f)** but not in **Fig. 5(g)** means that the strain was partially relaxed in these two grains.²⁹

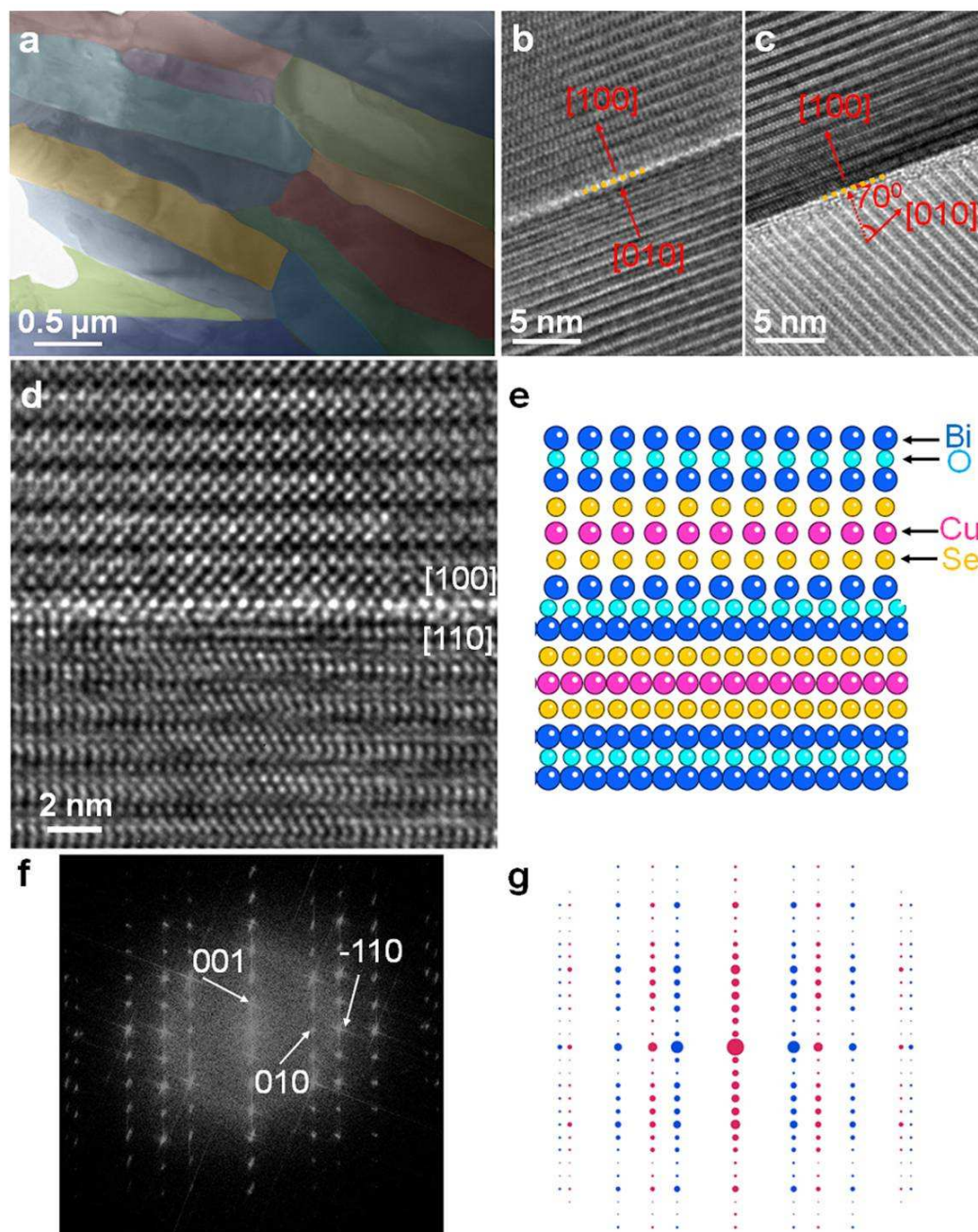


Fig. 5 Microstructures of pristine BiCuSeO sample: (a) Low magnification TEM image. (b) and (c) high resolution TEM images reveal two typical grain orientations. (d) The lattice image shows a good interface between two grains of the BiCuSeO sample. (e) atomic model of the two grains based on [100] (top) and [110] (bottom) directions. (f) and (g) are fast Fourier transform images of (d) and (e), respectively. Reproduced with permission from ref. 29. Copyright: 2013 Nature Publishing Group.

Thermoelectric transport properties of pristine BiCuSeO:

The properties of oxychalcogenides in the form of films and bulks were

investigated. The optoelectronic properties were mainly studied in the film forms, which were prepared by pulsed laser deposition (PLD)¹⁰³ and a reactive solid-phase epitaxial (R-SPE) technique, *etc.*¹⁰⁴ The bulk materials were usually prepared by a two-steps routine method: powders synthesis followed by pellets densification.^{27, 30} The single phase powders can be synthesized by hydrothermal method,¹⁰⁵ solid state reaction,⁹⁵ or mechanical alloying.^{106, 107} The as-synthesized powers can then be solidified into bulk by cold-pressing,^{29, 30} hot-pressing sintering,^{73, 108, 109} or spark plasma sintering.^{106, 110-113} It should be noted that the studies by several groups indicate that the thermoelectric properties vary depending on the densification methods, which probably originates from either density differences or preferential orientations of grains. Here, we only discuss the thermoelectric properties of BiCuSeO prepared by powders grinding followed by solid state sintering hereafter in this section.²⁹

As shown in the **Fig. 6(a)**, the electrical conductivity of BiCuSeO increases with rising temperature, indicating a semiconductor transport behavior. In the entire temperature range of the measurement, the electrical conductivity is much lower than that of state-of-the-art thermoelectric materials,^{1, 8, 12, 15, 32} for example, it is about 1.12 Scm^{-1} at room temperature, **Table 1**. The low electrical conductivity is related to the low carrier concentration of $1 \times 10^{18} \text{ cm}^{-3}$ and carrier mobility of $22 \text{ cm}^2\text{V}^{-1}\text{s}^{-1}$. **Fig. 6(b)** shows that the Seebeck coefficient of BiCuSeO is about $350 \mu\text{VK}^{-1}$ at room temperature, and keeps increasing with rising temperature and reaches about $425 \mu\text{VK}^{-1}$ at 923 K. The origin of the *p*-type conduction in pristine BiCuSeO is possibly related to the Cu vacancies, this will be discussed later. The combination of low electrical conductivity and large Seebeck coefficient results in a moderate power factor of about $2.5 \mu\text{Wcm}^{-1}\text{K}^{-2}$ at 923 K, **Fig. 6(c)**. The heat capacity, C_p , shows an increasing trend with temperature, **Fig. 6(d)**. As shown in **Fig. 6(e)**, the total thermal conductivity is low at room temperature, and keeps decreasing with rising temperature. The thermal conductivity is determined by its lattice part, since the electrical thermal conductivity is low. The lattice thermal conductivity is about $0.60 \text{ Wm}^{-1}\text{K}^{-1}$ at room temperature and decreases to $0.40 \text{ Wm}^{-1}\text{K}^{-1}$ at 923 K,²⁹ which is much lower than the values observed in

most thermoelectric materials.^{12, 13, 32} The origin of this low thermal conductivity will be discussed in the next section. The relatively low power factor, can be over compensated by the extremely low thermal conductivity, thus leading to a modest dimensionless figure-of-merit ZT value about 0.5 at 923K,²⁹ as shown in **Fig. 6(f)**. This ZT value indicates that BiCuSeO is a potential candidate for thermoelectric applications in the middle temperature range.

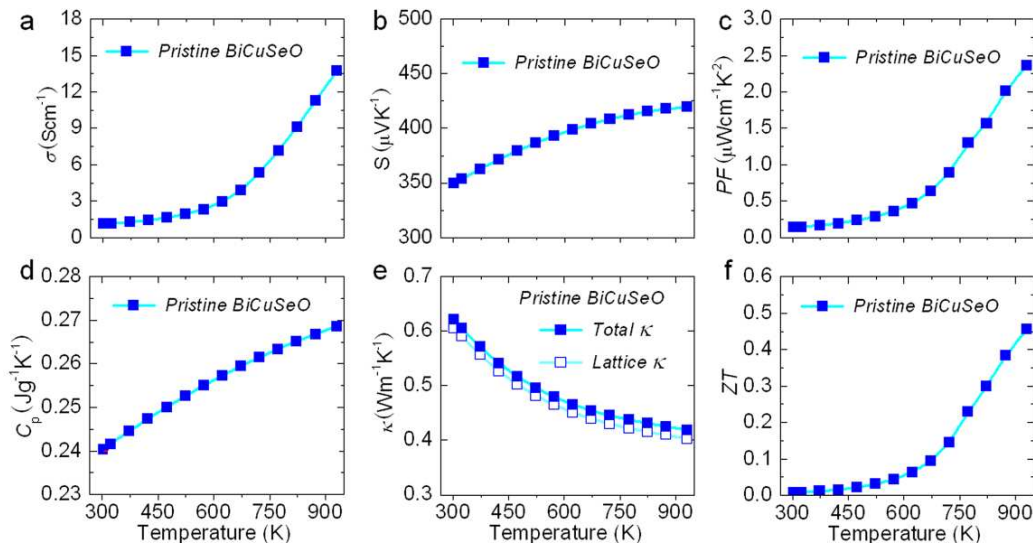


Fig. 6 Thermoelectric properties of pristine BiCuSeO. (a) Electrical conductivity. (b) Seebeck coefficient. (c) Power factor. (d) Heat capacity. (e) Total and lattice thermal conductivity. (f) Dimensionless figure-of-merit, ZT .

DOS effective masses:

The Seebeck coefficient of pristine BiCuSeO is large, *e.g.*, 350 μ V K⁻¹ at 300 K and 425 μ V K⁻¹ at 923K. Initially, the large Seebeck coefficient values were suggested to be related to its layered crystal structure. The alternating insulating (Bi₂O₂)²⁺ layers and conductive (Cu₂Se₂)²⁻ layers were supposed to form a natural superlattice, with a 2D confinement of the charge carriers.³⁰ Indeed, the natural layered structure of (Bi₂O₂)²⁺/(Cu₂Se₂)²⁻/(Bi₂O₂)²⁺ is very similar to the two-dimensional electron gas (2DEG) in SrTiO₃/SrTi_{0.8}Nb_{0.2}O₃/SrTiO₃ artificial multilayer structures, which exhibit a giant absolute value of Seebeck coefficient \sim 850 μ V K⁻¹ at 300 K.¹⁰² Despite of the complex nonparabolic multi-band structure in BiCuSeO, the single parabolic model could still be adopted to give an rough estimation of effective mass about 0.6 m_e ,²⁹

only keep in mind that this DOS effective mass is a mixed effective mass of multi-bands since there are at least two valence bands contributing the electrical transport properties,

Lee *et al.* were the first to determine the individual effective masses of the two valence bands for the BiCuSeO.¹¹⁴ The effective mass of the heavy band ($\sim 1.1 m_e$) was estimated by using Pisarenko relation:³²

$$S = \frac{8\pi^2 k_B^2 T}{3qh^2} m_d^* \left(\frac{\pi}{3p} \right)^{2/3} \quad (1)$$

where S is Seebeck coefficient, k_B is Boltzmann constant, T is absolute temperature, q is an electron charge, h is Plank constant, m_d^* is the effective mass at Fermi level, and p is the hole concentration. **Fig. 7(a)** shows the Seebeck coefficients of K doped BiCuSeO, and the effective mass can be estimated from the slope of $S \cdot p^{2/3}$ vs. T as in the inset of **Fig. 7(a)**. It is seen that the slope of $S \cdot p^{2/3}$ vs. T in the undoped BiCuSeO is much steeper than those in K-doped ones, indicating a large effective mass in undoped BiCuSeO, in which only the heavy band is regarded to involve in valence band and the effective mass is thus estimated to be $\sim 1.1 m_e$. The estimated DOS effective masses of the K doped BiCuSeO series are shown in **Fig. 7(b)**, K doping moves the Fermi level deep into the second valence band, inset of **Fig. 7(b)**. The increase in the effective mass along with the K doping evidences the nonparabolic feature of the light valence band. The effective mass of the nonparabolic second valence band is dependent on the carrier concentration:¹¹⁴

$$(m_d^*)^2 = (m_{d0}^*)^2 + 4 \frac{m_{d0}^*}{E_1} \left[\left(\frac{3}{8\pi} \right)^{2/3} \frac{h^2}{2} \right] p^{2/3} \quad (2)$$

where m_{d0}^* is the DOS effective mass at valence band mode (VBM), which can be determined by the extrapolation of a plot of $(m_d^*)^2$ vs. $p^{2/3}$, and E_1 is a constant which can be calculated by the slope of the plot. The DOS effective mass at the VBM of the light hole was estimated to be $0.18 m_e$. **Fig. 7(c)** indicates that the power factor of BiCuSeO is critically dependent on both the effective mass and the carriers concentration. Similar power factor enhanced enhancement was observed in the K and Na doped BiCuSeO.^{114, 115}

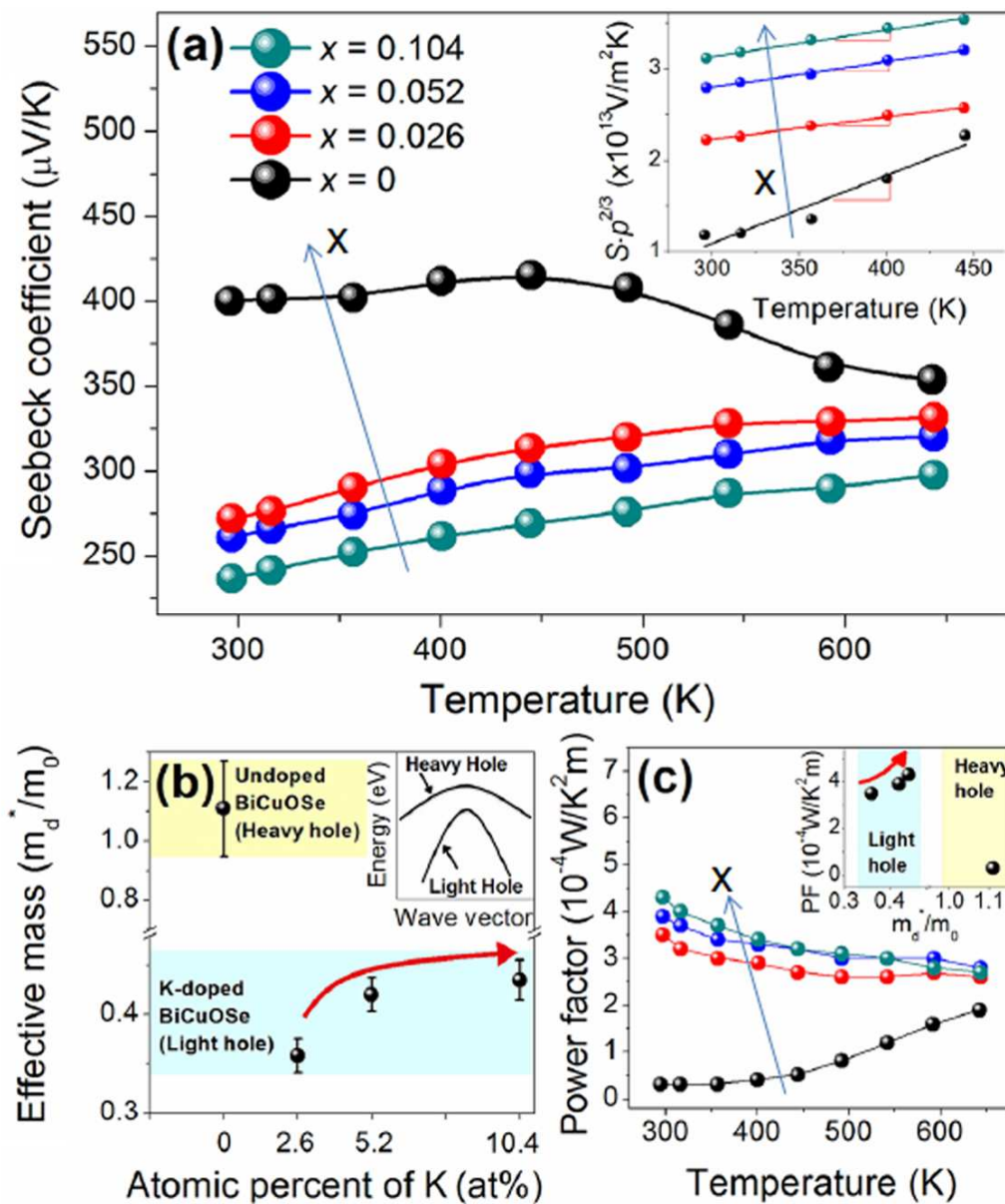


Fig. 7 Temperature-dependent Seebeck coefficient of the $\text{Bi}_{1-x}\text{K}_x\text{CuSeO}$ compounds. A plot of $S \cdot p^{2/3}$ vs. T is drawn in the inset for the estimation of the DOS effective masses based on Pisarenko relation. (b) Dependence of DOS effective masses on the atomic percent of K in the BiCuSeO compounds. A schematic for the two-band structure is shown in the inset. (c) Temperature-dependent thermoelectric power factors of the $\text{Bi}_{1-x}\text{K}_x\text{CuSeO}$ compounds. Room temperature power factors as a function of the effective mass are shown in the inset. Reproduced with permission from ref. 114. Copyright 2013, The American Physical Society.

Origin of the low thermal conductivity:

Even though the electrical transport properties are not as promising as the ones in state-of-the-art thermoelectric materials,^{12-14, 32} with power factor $S^2\sigma$ of 2.5

$\mu\text{Wcm}^{-1}\text{K}^{-2}$ at 923 K, the dimensionless figure-of-merit ZT can reach about 0.5 at 923 K. The promising ZT of pristine BiCuSeO is mainly due to its intrinsically low lattice thermal conductivity. As listed in **Table 1**, the lattice thermal conductivity is about $0.60 \text{ Wm}^{-1}\text{K}^{-1}$ at room temperature and decreases to as low as $0.40 \text{ Wm}^{-1}\text{K}^{-1}$ at 923 K. To clarify the origin of the intrinsically low thermal conductivity, the elastic properties of BiCuSeO compounds have been analyzed.^{29, 110} Young's modulus (E) value of BiCuSeO can be extracted from the longitudinal (v_l) and transverse (v_s) sound velocities.^{24, 29, 110} Young's modulus is related to the stiffness of a material's individual atomic bonds.²⁴ Weaker bonds of interatomic bonding generally result in lower stiffness, and lower Young's modulus. The materials with lower Young's modulus are considered as having “soft” bonding, which will result in a slow transport for phonons, thus in lower lattice thermal conductivity.¹¹⁶ Indeed BiCuSeO exhibits a low sound velocity (**Fig. 8(a)**), Young's modulus (**Fig. 8(b)**) and lattice thermal conductivity (**Fig. 8(c)**) at 300 K than some peer oxygen containing samples,^{117, 118} namely, the parameters (2107 ms^{-1} , 76.5 GPa , $0.9 \text{ Wm}^{-1}\text{K}^{-1}$) of BiCuSeO are lower, in compared to those (2901 ms^{-1} , 109.4 GPa , $1.4 \text{ Wm}^{-1}\text{K}^{-1}$) of $\text{Ba}_2\text{YbAlO}_5$, (3078 ms^{-1} , 116.5 GPa , $1.8 \text{ Wm}^{-1}\text{K}^{-1}$) of BaDyAlO_5 and (3832 ms^{-1} , 234.3 GPa , $2.2 \text{ Wm}^{-1}\text{K}^{-1}$) of $\text{Gd}_2\text{Zr}_2\text{O}_7$.^{29, 110}

Besides the analysis of Young's modulus (E), which relates to chemical bonding strength, the Grüneisen parameter (γ) is also relevant in evaluating the thermal conductivity.^{20, 119} The Grüneisen parameter is often referred as a temperature dependent anharmonicity parameter that reflects the phonon vibrations in crystal lattices that deviates from harmonic oscillation. Anharmonicity of the chemical bond drives the phonon-phonon umklapp and normal processes that intrinsically limit the lattice thermal conductivity. The Grüneisen parameter of BiCuSeO can be calculated using the following relationship:^{29, 120}

$$\gamma = \frac{3}{2} \left(\frac{1 + \nu_p}{2 - 3\nu_p} \right) \quad (3)$$

where Poisson ratio ν_p can be derived from the longitudinal v_l and transverse v_s sound velocities by:^{117, 120}

$$\nu_p = \frac{1 - 2(\nu_s/\nu_l)^2}{2 - 2(\nu_s/\nu_l)^2} \quad (4)$$

The Grüneisen parameter γ was calculated to be ~ 1.5 for BiCuSeO, which indicates a high anharmonicity of the lattice vibrations and is a signature of a low thermal conductivity material. The Grüneisen parameter (γ) value of ~ 1.5 for BiCuSeO is comparable or even a little bit higher than that (1.45) of PbTe,¹²¹ which is a conventional thermoelectric material that has been paid extensive attention. Morelli *et al.* reported that the intrinsically low thermal conductivity of AgSbTe₂ results from an extremely high Grüneisen parameter (γ) value of 2.05.²⁰ The high Grüneisen parameter (γ), linking to the bond anharmonicity, may originate from the presence of the lone pair electrons in the Sb's *sp*-hybridized orbitals.^{20, 122} This lone-pair electron, give rise to extra electron clouds surrounding Sb atoms and cause nonlinear repulsive forces which is manifested as bond anharmonicity.^{20, 122} As in the same V group, similarly low lattice thermal conductivity should be observed in the Bi-based compounds.^{120, 122} The connection between the nature of the bonding and the Grüneisen parameter (γ) has been explored in detail theoretically by Huang *et al.*,¹²³ who clearly show the effect of large electron clouds on anharmonicity. In addition, the lone pair electrons of Bi probably lead to a more asymmetric electron density thus in stronger lattice anharmonic vibration. The very low thermal conductivity and high Grüneisen parameter (γ) value of 1.5 in BiCuSeO system arises at least partially due to the increased bond anharmonicity associated with the occurrence of trivalent Bi.¹²⁰⁻¹²²

Besides the analysis of Young's modulus and Grüneisen parameter for the BiCuSeO system, other possible reasons were also suggested, including the layered structure where phonons might be confined and scattered at the interfaces,¹²⁴ the presence of heavy elements which leads to lower phonon group velocity, *etc.*^{13, 14} All these features can be shortly summarized as involving heavy atoms with 'soft' bonding, which can meet the requirements for a low thermal conductivity materials selection as suggested by Clarke.¹¹⁶

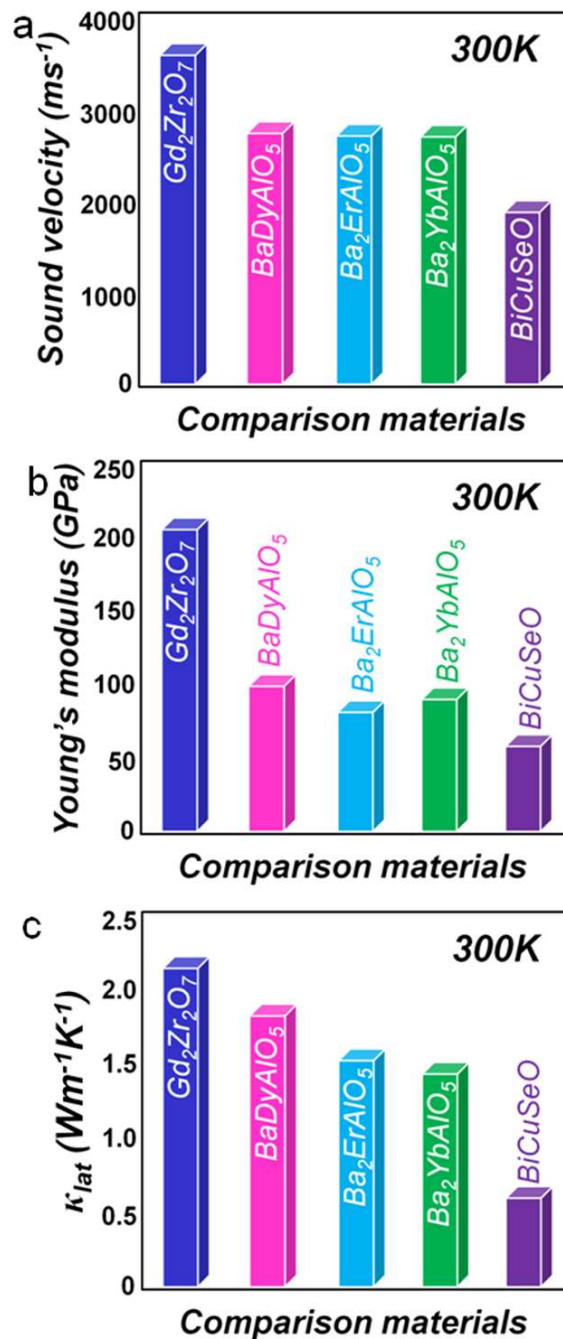


Fig. 8 (a) Sound velocity comparison for $BiCuSeO$ and typical oxygen containing materials. (b) Young's modulus comparison for $BiCuSeO$ and typical oxygen containing materials. (c) Room temperature lattice thermal conductivity comparison for $BiCuSeO$ and typical oxygen containing materials.

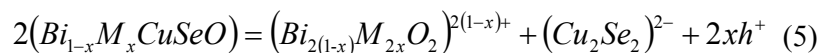
3. Enhanced thermoelectric performance of $BiCuSeO$ through optimizing charge carriers concentration

Compared with state-of-the-art thermoelectric materials,^{12-14, 32} the features of pristine BiCuSeO can be summarized as a moderate Seebeck coefficient, intrinsically low lattice thermal conductivity, but low electrical conductivity. At a first glance, it seems that there is not too much room left to further reduce the lattice thermal conductivity, which is already low and ranges from $0.40 \text{ Wm}^{-1}\text{K}^{-1}$ to $0.60 \text{ Wm}^{-1}\text{K}^{-1}$ at 300-923 K. Therefore, the best way to enhance the thermoelectric figure of merit ZT seems to improve the electrical transport properties. The room temperature carriers concentration is about $1 \times 10^{18} \text{ cm}^{-3}$, which is much lower than the optimum values observed in state-of-the-art thermoelectrics,^{12-14, 32} which are generally of the order of $1 \times 10^{19} \sim 1 \times 10^{20} \text{ cm}^{-3}$.³² The positive Seebeck coefficient indicates that holes are the majority carriers. Therefore, several options can be followed to increase the carriers concentration. Although BiCuSeO cannot be described using an “ionic-model”, as it can be seen from the strong hybridization between Cu and Se orbitals in the band structure calculations, **Fig. 3**, such a simplified model can still be useful to understand the doping behavior in this compound.⁹⁹ In this model, to keep the charge balance in the BiCuSeO, valent configuration of Bi is 3+, Cu 1+, both Se and O 2-. Therefore, the elements with positive valence < 3 can be selected as p-type dopants on Bi sites, while no elements with positive valence < 1 could substitute Cu site. For the Se and O sites, the elements with negative charge must be > 2 , which offers few options. Thus, to improve the electrical transport properties of BiCuSeO, most of elements with 2+ valence (M^{2+}) were extensively studied, examples are alkaline-earth metals: Mg, Ca, Sr and Ba.^{26, 27, 29, 30} In this section, we summarize the thermoelectric transport properties for $\text{Bi}_{1-x}\text{M}_x\text{CuSeO}$.

Carrier concentration and carrier mobility for $\text{Bi}_{1-x}\text{M}_x\text{CuSeO}$:

Fig. 9(a) shows the schematic crystal structure of BiCuSeO, which depicts that the holes generated by M^{2+} ($M = \text{Mg, Ca, Sr and Ba}$) doping into Bi sites are injected into $(\text{Cu}_2\text{Se}_2)^{2-}$ metallic layers.^{26, 27, 29-31} This behavior can be described similarly to that of iron-based LaFeAsO superconductors.⁸⁸ In a simplified picture, BiCuSeO materials consist of insulating oxide $(\text{Bi}_2\text{O}_2)^{2+}$ layers with ionic bonds, acting as charge reservoirs,

and conductive selenide $(\text{Cu}_2\text{Se}_2)^{2-}$ layers with covalent bonds, serving as the conduction pathway for carriers transport. Therefore, the carriers concentration can be enhanced through partial substitution of Bi^{3+} by M^{2+} in the insulating oxide $(\text{Bi}_2\text{O}_2)^{2+}$ layers, and the induced holes then transfer to the conductive $(\text{Cu}_2\text{Se}_2)^{2-}$ layers. This can be explained by a defect equation as follows:^{26, 27, 29, 30}



This simplified description is well supported by the band structure calculations. Indeed, one can see above that Bi and O states are located well below the Fermi level, and that the top of the valence band consists in hybridized Cu and Se states. Therefore, when some holes are created within the Bi_2O_2 layers they are transferred to the Cu-Se states, at the top of the valence band.^{99, 125} Moreover, the calculations have shown that M^{2+} substitutions on the Bi site does not influence the states located close to the Fermi level and that the doping can be described in the framework of a rigid band model.⁹⁹ Therefore, M^{2+} doping on the Bi site only changes the Fermi energy, and thus the charge carriers concentration.

As shown in **Fig. 9(b)**, the carriers concentration are significantly increased after M^{2+} ($\text{M} = \text{Mg}, \text{Ca}, \text{Sr}$ and Ba) doping.^{26, 27, 29, 30} a value as high as $1.3 \times 10^{21} \text{ cm}^{-3}$ can be reached at a 15% M^{2+} doping level. According to the equation (5), which corresponds to the rigid band model, if we assume that each M^{2+} gives one hole h^+ to the valence band, with $x = 0.15$ M^{2+} doping there should be 0.3 holes per unit cell (2 BiCuSeO unit per unit cell), and based on the volume of the BiCuSeO unit cell, which is around 137.06 \AA^3 (**Table 1**), it should lead to a theoretical carriers concentration around $1.1 \times 10^{21} \text{ cm}^{-3}$. The experimental value agrees very well the estimation, which confirms the validity of the rigid band model framework for these materials. It should be noted that not all M^{2+} elements are effective dopants. Indeed, the carriers concentration obtained by Mg^{2+} doping is two orders of magnitude lower than those of M^{2+} ($\text{M} = \text{Ca}, \text{Sr}$ and Ba),^{26, 27, 29, 30} and is much lower than aforementioned calculated value, indicating that not all Mg atoms effectively replacing Bi^{3+} in the BiCuSeO lattice. This phenomenon might be explained by the facts that Mg^{2+} is much smaller than Bi^{3+} , Ca^{2+} , Sr^{2+} , and

Ba^{2+} thus has a smaller overlap of the atomic orbitals and a lower charge transfer.²⁶

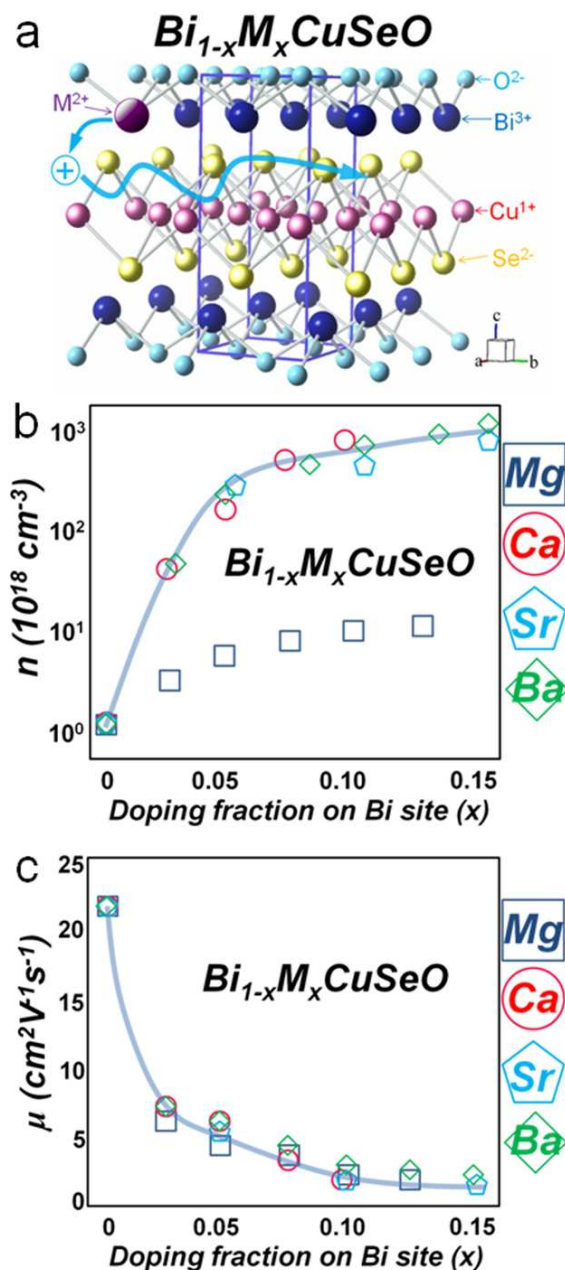


Fig. 9 (a) Schematic crystal structure of BiCuSeO , in which hole carriers generated by M^{2+} ($\text{M} = \text{Mg}, \text{Ca}, \text{Sr}, \text{and Ba}$) doping into Bi sites are injected into CuSe metallic layers as a result of the large energy offset between these two layers. (b) Carrier concentration of BiCuSeO as a function of M^{2+} doping fractions. (c) Carrier mobility of BiCuSeO as a function of M^{2+} doping fractions.

Compared with the state-of-the-art thermoelectric materials,^{12-14, 32} the carrier mobility of pristine BiCuSeO is relatively low, around $\sim 22 \text{ cm}^2 \text{ V}^{-1} \text{ s}^{-1}$ at room temperature. As shown in **Fig. 9(c)**, the carriers mobility shows a pronounced decrease

with rising M^{2+} doping fractions, from $22 \text{ cm}^2\text{V}^{-1}\text{s}^{-1}$ for pristine BiCuSeO to about $1\sim 2 \text{ cm}^2\text{V}^{-1}\text{s}^{-1}$ for the samples with $0.15 M^{2+}$ ($M = \text{Mg}, \text{Ca}, \text{Sr}$ and Ba) doping.^{26, 27, 29, 30} This dramatic decrease of carrier mobility can be well explained by the increased ionized impurity scattering.

Thermoelectric transport properties for $\text{Bi}_{1-x}\text{M}_x\text{CuSeO}$:

In this section, the thermoelectric properties of $\text{Bi}_{1-x}\text{M}_x\text{CuSeO}$ ($M = \text{Mg}, \text{Ca}, \text{Sr}$ and Ba) are compared,^{26, 27, 29, 30} and only the samples exhibiting the highest ZT values were selected. It should be underlined that all transport properties of BiCuSeO polycrystalline samples must be measured along the same direction since BiCuSeO exhibits a layered structure leading to platelet grains, the ZT will be overestimated by 25-30% if the measurement directions were wrong in BiCuSeO system.⁷³ A good example of possible measurement errors are found in Bi_2Te_3 alloys, which crystallize in a layered structure too. In Bi_2Te_3 single crystals, the electrical conductivity and thermal conductivity perpendicular to the c -axis are about 4 and 2 times larger than those along the c -axis, respectively.¹²⁶ If the thermoelectric properties were measured along the different directions, in other words, the thermal and electrical conductivities were measured along out-of plane and in-plane directions, respectively.¹²⁷ Thus the final ZT was overestimated by 50% due to the texture in polycrystalline materials.

As shown in **Fig. 10(a)**, BiCuSeO exhibits low electrical conductivity over the entire temperature range from 300 K to 923 K, and a semiconducting behavior. Upon M^{2+} doping, the electrical transport changes to a metallic behavior and the electrical conductivity shows a significant increase with rising M^{2+} doping fractions. The highest electrical conductivity is obtained in 0.125 Ba doped sample.²⁷ 0.05 Mg doping improves the electrical conductivity but only with very limited effect, which is consistent with the aforementioned low doping efficiency of Mg.²⁶ The M^{2+} doping also decreases the Seebeck coefficient, as shown in **Fig. 10(b)**. The Seebeck coefficient values of BiCuSeO range from $\sim 350 \mu\text{VK}^{-1}$ at 300 K to $\sim 425 \mu\text{VK}^{-1}$ at 923 K, and decrease down to $\sim 69 \mu\text{VK}^{-1}$ at 300 K and $\sim 167 \mu\text{VK}^{-1}$ at 923 K upon 0.125 Ba doping,²⁷ owing to the significantly increased carriers concentration. **Fig. 10(c)** shows

that all power factor curves increase monotonously up to 923 K, and can be enhanced with carrier concentration optimizing. The lattice thermal conductivity for BiCuSeO is intrinsically low and ranges from $0.40 \text{ Wm}^{-1}\text{K}^{-1}$ to $0.60 \text{ Wm}^{-1}\text{K}^{-1}$ at 300-923 K. However, the lattice thermal conductivity can be further reduced by M^{2+} doping, **Fig. 10(d)**. The reduction of the lattice thermal conductivity has been well explained by point defect scattering based on Callaway model, in which the point defects scattering in a solid solution system originates from both the mass difference (mass fluctuations) and the size and the interatomic coupling force differences (strain field fluctuations) between the impurity atom and the host lattice.^{29, 117} Apart from the point defect scattering, the lattice thermal conductivity also can be further reduced, i.e., lattice thermal conductivity was reduced to $\sim 0.25 \text{ Wm}^{-1}\text{K}^{-1}$ at 923 K as the grain size was reduced to 200-400 nm for Ba^{2+} doped samples.²⁷

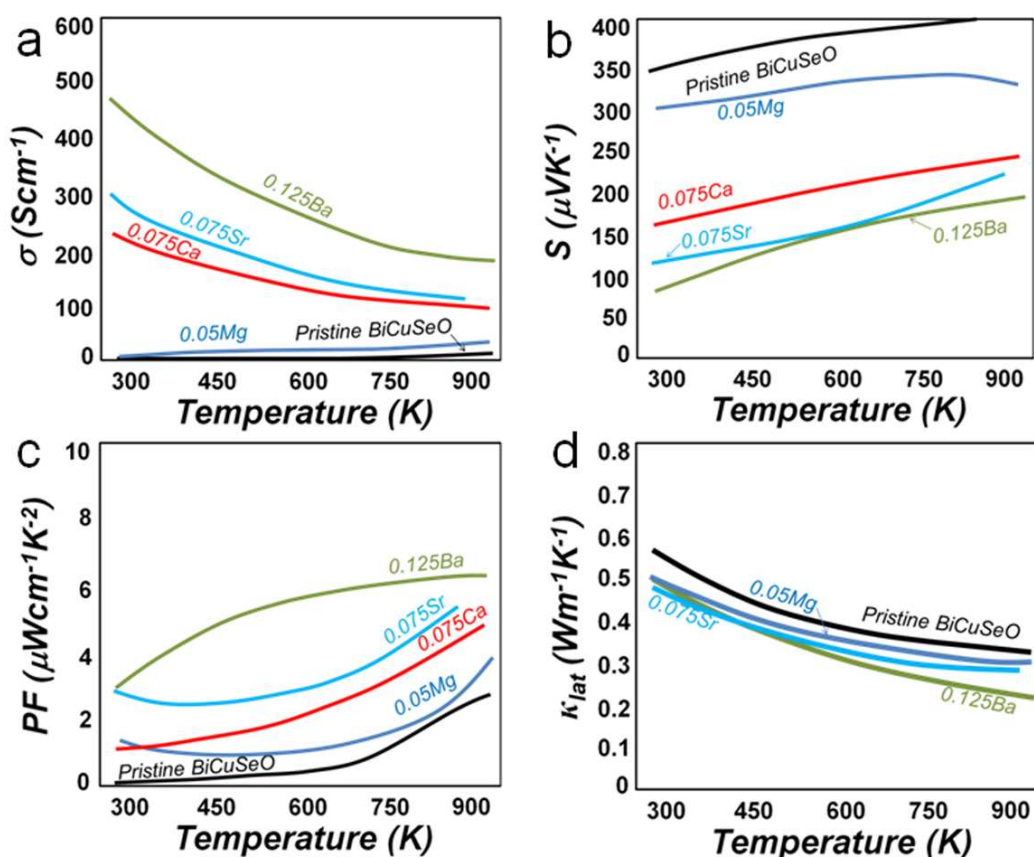


Fig. 10 Thermoelectric properties of M^{2+} ($M = \text{Mg}, \text{Ca}, \text{Sr},$ and Ba) doped BiCuSeO. (a) Electrical conductivity. (b) Seebeck coefficient. (c) Power factor. (d) Lattice thermal conductivity.

Fig. 11 shows the temperature dependent dimensionless figure-of-merit, ZT , for the

$\text{Bi}_{1-x}\text{M}_x\text{CuSeO}$ systems ($M = \text{Mg}, \text{Ca}, \text{Sr}, \text{and Ba}$).^{26,27,29,30} Here, it should be noted that the thermoelectric properties of some BiCuSeO systems were measured up to 923 K, some others not. The reasons may be the instruments limit. To dig the potential properties at elevated temperatures, one can coat the sample with a thin (0.1-0.2 mm) layer of boron nitride (BN) to protect instruments, the operating details can be referenced in literature.³⁹ From **Fig. 11**, it can be seen that the ZT has been significantly improved from 0.5 for pristine BiCuSeO to 0.67, 0.9, 0.76, and 1.1 for Mg, Ca, Sr, and Ba doped samples, respectively.^{26,27,29,30} These achievements are impressive for a new candidate since the ZT of unity has been a threshold value for several decades until the nanotechnology was discovered in the 1990s.^{12-14,32}

Apart from optimizing the electrical conductivity through doping with alkaline-earth metals, i.e., Mg, Ca, Sr, Ba,^{26,27,29,30} the alkali metals (Na and K) are also confirmed to be promising owing to their similar ionic size as alkaline earth ones,^{114,128} only differing in the sense that two extra holes, instead of one, can be introduced for each alkali-metal substitution. However, the limited solubility of alkali metals in BiCuSeO impedes their applications in BiCuSeO as effective acceptors. As a result, the power factor of alkali metals doped compositions shows a decreasing trend with rising temperature, as comparing to those of alkaline earth metals doped $\text{Bi}_{1-x}\text{M}_x\text{CuSeO}$.

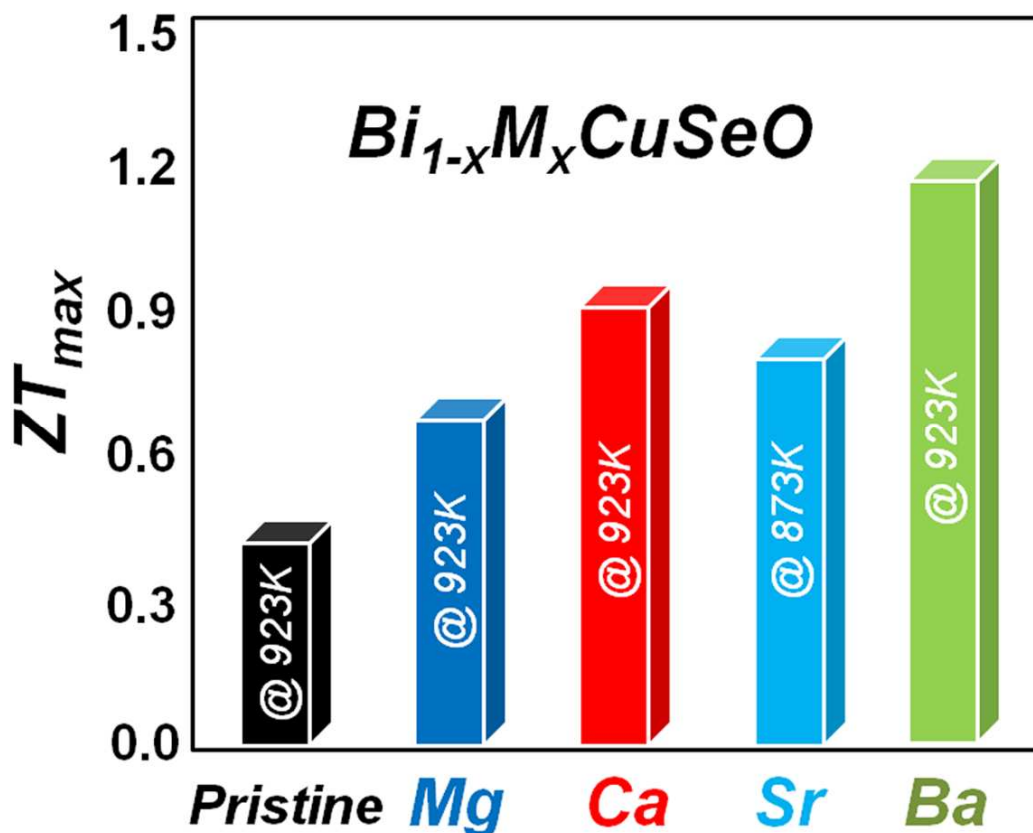


Figure 11: Dimensionless figure-of-merit ZT for the $\text{Bi}_{1-x}\text{M}_x\text{CuSeO}$ ($M = \text{Mg}, \text{Ca}, \text{Sr}, \text{and Ba}$) systems.^{26, 27, 29, 30}

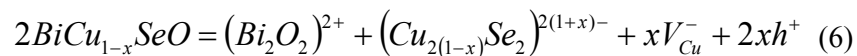
4. Other methods to enhance the thermoelectric performance of BiCuSeO

Other than charge carriers concentration optimization *via* M^{2+} doping, decreasing the grains size, producing Cu vacancies, doping with Pb, tuning band gap, and increasing carrier mobility through grains texturation are also proved to be effective to enhance the thermoelectric performance in BiCuSeO system.

Increasing performance by optimizing Cu vacancies:

In this section, we shall describe an effective way to achieve high thermoelectric performance by introducing Cu deficiencies.¹¹¹ It is generally believed that Cu vacancies widely exist in BiCuSeO synthesized during the various processes.¹²⁹ Here is the first example of study devoted to the use of Cu vacancies to dope BiCuSeO and

optimize the carriers concentration. **Fig. 12(a)** depicts a schematic crystal structure of BiCuSeO with Cu deficiencies. In contrary to M^{2+} doping, the holes are directly generated in the conductive $(Cu_2Se_2)^{2-}$ layers due to Cu vacancies. In a simplified ionic model, this can be expressed by a defect equation as follows:¹¹¹



where V_{Cu}^- is Cu vacancy, and h^+ is the generated holes. This equation implies that Cu deficiencies can increase the hole concentration just like conventional acceptors.

As shown in **Fig. 12(b)**, the samples with Cu deficiency ($x < 0.1$, the solubility limit may be smaller than this) exhibit significantly enhanced electrical conductivity, e.g., the electrical conductivity of BiCu_{0.975}SeO is $5.3 \times 10^3 \text{ Sm}^{-1}$ at 923 K, one order of magnitude higher than 470 Sm^{-1} of pristine BiCuSeO. The introduction of Cu deficiencies also significantly decreases Seebeck coefficient, as shown in **Fig. 12(c)**. Upon the formation of Cu deficiencies, the Seebeck coefficient decreases due to the increased holes concentration, but the values still maintain between $165 \mu\text{VK}^{-1}$ and $323 \mu\text{VK}^{-1}$ over the entire temperature range of the measurement. **Fig. 12(d)** shows that the thermal conductivity for BiCu_{1-x}SeO almost independent on the fraction of Cu deficiencies up to $x = 0.025$, while the thermal conductivity starts to increase as the Cu deficiency fraction x exceeds 0.025 due to the growing contribution from the electronic thermal conductivity. **Fig. 12(e)** shows that ZT increases with temperature, reaches a maximum ~ 0.81 at 923 K in BiCu_{0.975}SeO. The thermoelectric properties comparison between samples with Cu deficiencies and pristine one are shown in the inset of **Fig. 12(e)** (pristine BiCuSeO is marked by the subscript symbol o), unambiguously shows that the obtained ZT enhancement is mainly due to the improved electrical conductivity. The results indicate that the thermoelectric properties of BiCuSeO can be remarkably improved by optimizing hole concentrations through tuning the fractions of Cu deficiencies in the conductive $(Cu_2Se_2)^{2-}$ layers.¹¹¹

To explore the mechanisms associated with charge and heat transport in BiCu_{1-x}SeO with Cu deficiencies. Xu *et al.* carried out electronic structures calculations of both the ground and excited states based on density functional theory (DFT) using a

$2 \times 2 \times 2$ supercell and a composition $\text{BiCu}_{0.9375}\text{SeO}$,¹³⁰ here it should be noted that $2 \times 2 \times 2$ supercell is not big enough to estimate the band structures of a doped BiCuSeO system and calculation uncertainty may be caused. As Cu deficiencies are introduced into the structure, dramatic changes in the electronic structures are revealed by DFT calculations, which are consistent with the x-ray absorption near-edge spectroscopy (XANES) measurements. The projected DOS and the electronic configurations of the $\text{BiCu}_{1-x}\text{SeO}$ system indicate that Cu deficiencies may significantly enhance the charge transfer among Bi atoms and among Se atoms, but have nearly no effects on Cu and O atoms. **Fig. 12(f)** shows the charge transfer difference between $\text{BiCu}_{1-x}\text{SeO}$ and BiCuSeO is 0.02 among Bi atoms and 0.03 among Se atoms, respectively. Whereas, the charge transfers among Cu atoms and O atoms in $\text{BiCu}_{1-x}\text{SeO}$ can be considered the same as those in BiCuSeO . The existence of an interlayer charge transfer route involving the Bi-Se chain along the c axis is probably the origin of the high performance of $\text{BiCu}_{1-x}\text{SeO}$ system. Besides the growing contribution from the electronic thermal conductivity, another explanation of the increasing thermal conductivity with rising fraction of Cu deficiencies was proposed, that is Cu deficiencies as well as the enhanced interlayer charge transfer between the Se and Bi atoms might affect the polarizability of the Bi $6s^2$ electron lone pairs and relieve the bond anharmonicity, thus result in an increased lattice thermal conductivity. The calculation by Xu *et al.* reveals that the increase in conductivity in $\text{BiCu}_{1-x}\text{SeO}$ via Bi-Se linkages is quite inspiring and may further evidence BiCuSeO as a promising thermoelectric material.¹³⁰

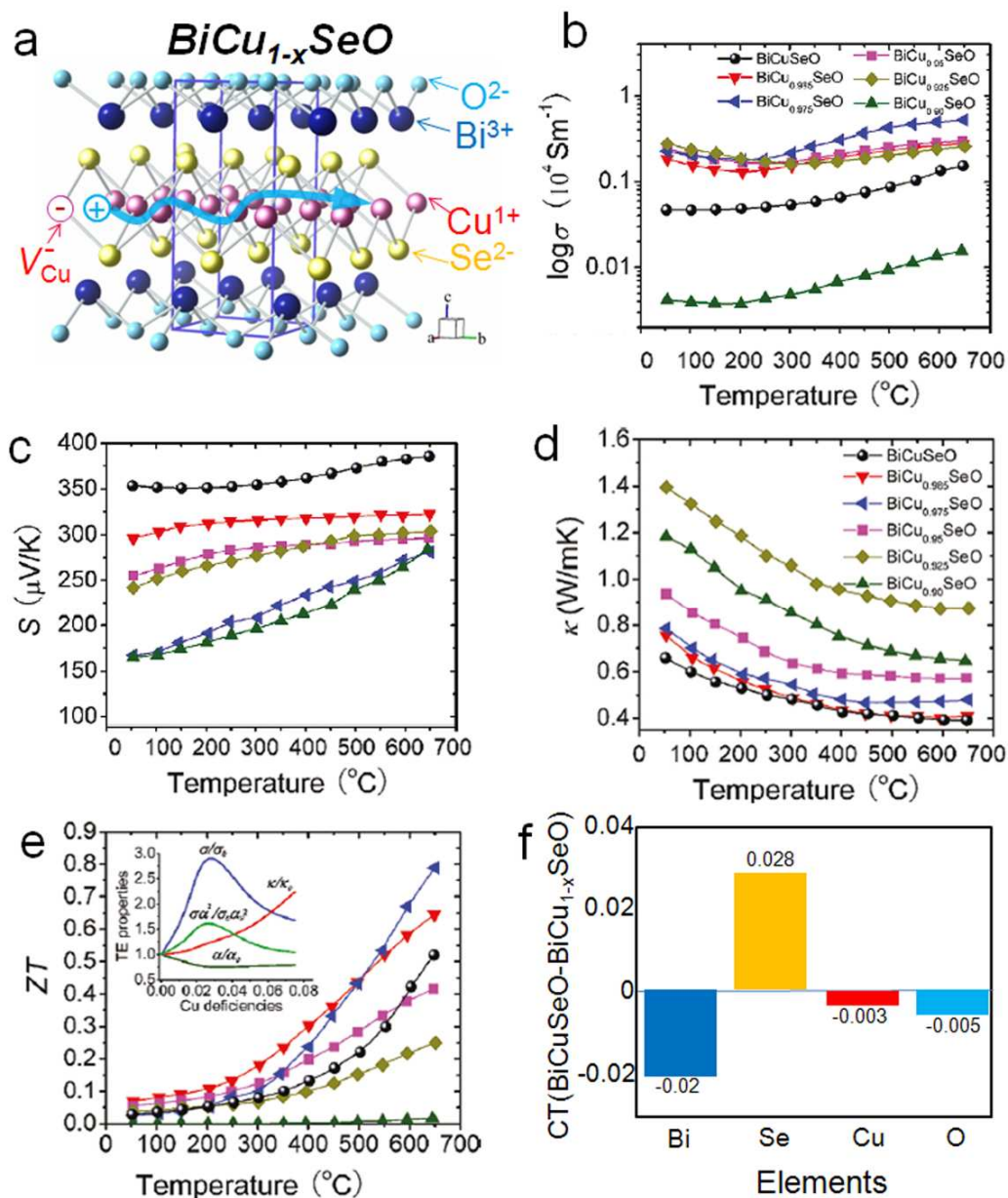


Fig. 12 (a) Schematic crystal structure of BiCuSeO, in which hole carriers are generated by Cu vacancies. Temperature dependence of (b) electrical conductivity. (c) Seebeck coefficient. (d) total thermal conductivity. (e) Dimensionless figure-of-merit ZT of BiCu_{1-x}SeO. The inset in (b) shows the normalized thermoelectric properties of BiCu_{1-x}SeO samples at 923K as a function of Cu vacancies concentration. (f) Difference between the charge transfers of the atoms of BiCuSeO and vacancy-doped BiCu_{1-x}SeO. The vacancies significantly change the charge transfer of the Bi and Se atoms, while those of Cu and O remain largely the same. Reprinted (adapted) with permission from (ref 111). Copyright (2011) American Chemical Society. Ref. 130 reproduced by permission of The Royal Society of Chemistry.

Improving performance via simple and facile ball milling:

Although the thermal conductivity in pristine BiCuSeO is already extremely low, there is still room left for further reduction. Li *et al.* reported that a simple ball milling process could cause a remarkable enhancement on thermoelectric properties for pristine BiCuSeO. A ZT value up to ~ 0.70 at 773 K was achieved, which mainly comes from the composition homogeneity improvement and grain size refining during the ball milling process.¹¹⁰

As shown in **Fig. 13(a)** and **Fig. 13(b)**, the grain size of BiCuSeO was significantly reduced to 1-2 μm from 10-20 μm by 1500 min ball milling. Both total (**Fig. 13(c)**) and lattice thermal conductivity (inset of **Fig. 13(a)**) exhibit the same decreasing trend with increasing temperature. The lattice thermal conductivity above 700 K shows a significant decrease after ball milling process, stemming mainly from the enhanced grain boundary scattering due to the refined grain size by ball milling.

It is usually believed that the electrical conductivity would be diminished with reduced grain size due to the intensified charge carrier scattering at the grain boundaries. However, it is not the case for ball-milled BiCuSeO. **Fig. 13(d)** shows that the carrier mobility was indeed reduced by ball milling and would be further reduced with prolonged ball milling time, whereas, the carrier concentration was found to increase after ball milling process, showed an enhancing trend with prolonging ball milling time from 500 min from 1500 min. The carrier concentration at room temperature was increased from $2.65 \times 10^{17} \text{ cm}^{-3}$ to $5.22 \times 10^{18} \text{ cm}^{-3}$ after 500 min ball milling, and further to $2.73 \times 10^{19} \text{ cm}^{-3}$ after 1500 min ball milling.¹¹⁰ Although the reason for the increased carrier concentration by ball milling was not mentioned in the report, but they are most certainly come from the introduced Cu vacancies, that form easily during the synthesis process.¹⁰⁸ Similar phenomenon was observed in Bi_2Te_3 ,^{126, 131} whose carrier concentration was recognized to be sensitive to the crystal defects aroused from the ball milling process. The acceptor crystal defects came from the broken layered structures through mechanical stress during ball milling process, thus the carrier concentration would be increased accordingly. **Fig. 13(e)** shows that the electrical conductivity of BiCuSeO was strongly improved after ball milling, especially at high temperatures, and that the electrical conductivity was

further increased when the ball milling time was prolonged from 500 min to 1500 min. All the electrical conductivity behaviors are consistent with the observed carrier concentration variations, evidencing that ball milling is responsible for the electrical conductivity enhancement, by unintentional doping.

Benefiting from the strongly enhanced electrical conductivity and lowered thermal conductivity, the ZT value was lifted up to ~ 0.70 at 773 K for BiCuSeO with 500 min ball milling process, as shown in **Fig. 13(f)**, this value is about 3.5 times higher than its pristine counterpart. It is quite astonishing that a simple ball milling process could cause such a remarkable enhancement on thermoelectric performance for pristine BiCuSeO. This enhancement originates from the improved electrical conductivity, which is due to unintentional doping leading to an increased carriers concentration, but also to the reduced lattice thermal conductivity linked to the large grain boundaries concentration. The work reported by Li *et al.* also indicated a good anti-oxidation feature of BiCuSeO, because the single phase powders were ball milled in air without any protective atmospheres.¹¹⁰ Later, this anti-oxidation feature of BiCuSeO was further evidenced by the successful synthesis of single-phase BiCuSeO powders by mechanical alloying in air.^{106, 107} This advantage of anti-oxidation feature of BiCuSeO outperforms most of these state-of-the-art thermoelectric materials.^{12-14, 32}

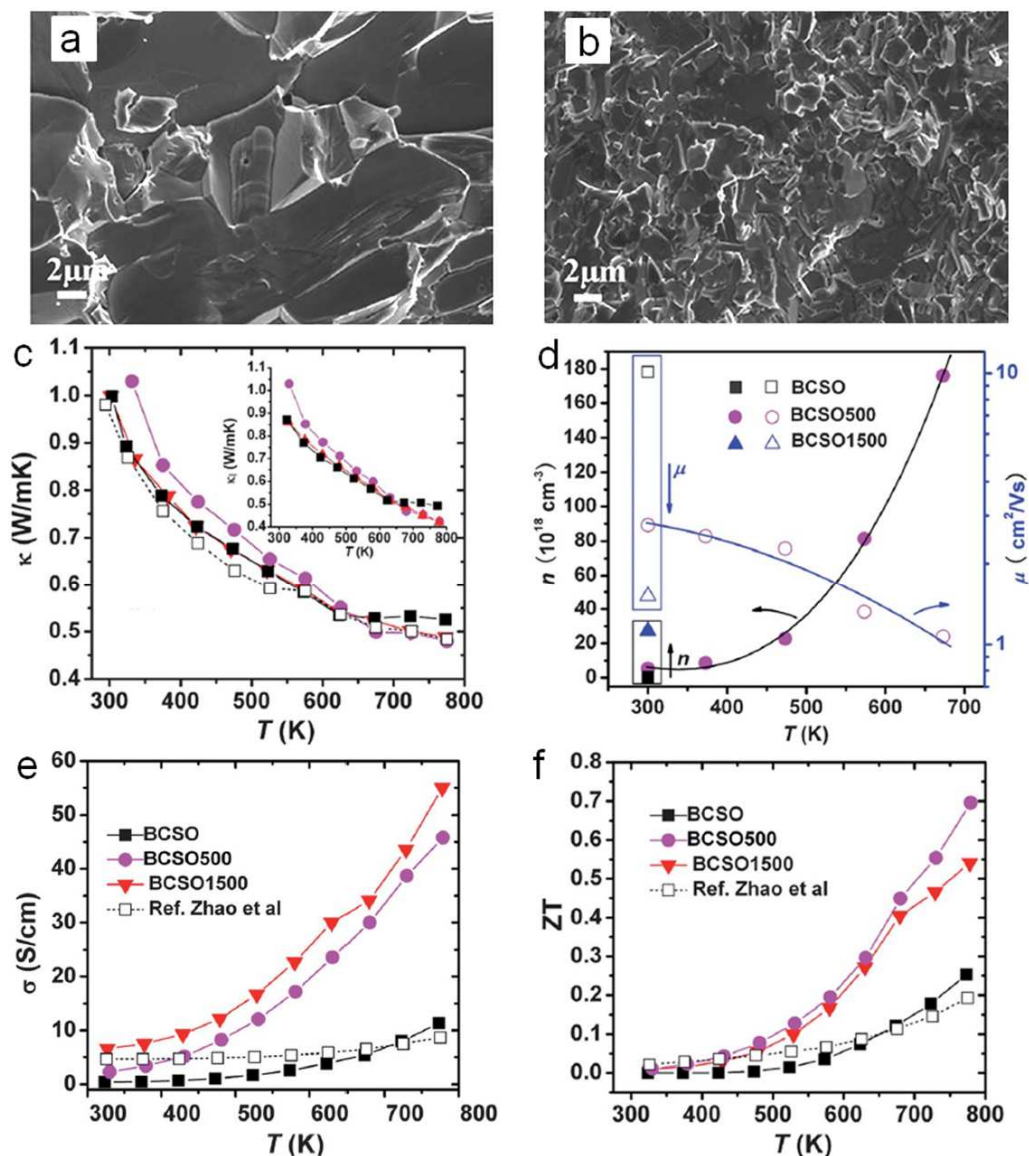


Fig. 13 Temperature dependence of thermoelectric transport properties of BiCuSeO with different milling times, data from ref³⁰ are also given for comparison. (a) SEM fractograph for BiCuSeO without ball milling treatments. (b) SEM fractograph for BiCuSeO with ball milling 1500 min. (c) Total thermal conductivity and (inset) the lattice thermal conductivity. (d) Electrical conductivity. (e) Carrier concentration (n) and the carrier mobility (μ). (f) Dimensionless figure-of-merit ZT . Ref. 110 Reproduced by permission of The Royal Society of Chemistry.

Increasing performance through multifunctional Pb doping:

Besides alkaline-earth anions M^{2+} ($M = \text{Mg}, \text{Ca}, \text{Sr}$ and Ba) doping on Bi^{3+} sites, Pb^{2+} doping has been extensively studied in several groups,^{106, 108, 112, 132} which is also an effective method to enhance the thermoelectric performance of BiCuSeO. Although the function of Pb^{2+} doping resembles that of alkaline-earth metals doping to the most

extent, we'd like to introduce Pb^{2+} doping in this separate section since some distinct mechanisms were also noticed.

Lan *et al.* observed some 5-10 nm nanodots in Pb^{2+} doped BiCuSeO under TEM, however, the composition of these nanodots were not well identified yet,¹¹² although the over-doping Pb is most suspicious. These nanodots provided excessive phonon scattering centers and thus greatly reduced the lattice thermal conductivity. Lan *et al.* also found that the carrier concentration and the carrier mobility were enhanced simultaneously by Pb^{2+} doping, both of which kept an increasing trend with Pb^{2+} doping fraction.¹¹² The normalized carrier mobility, $\mu(m^*)^{3/2}$, was evaluated to investigate the origin of the enhancement of thermoelectric performance. The DOS effective mass (m^*) was derived through experimentally fitting the dependence of Seebeck coefficient on carrier concentration, within a single parabolic band model. The results showed that the DOS effective mass was increased from $1.7 m_0$ (m_0 is the rest mass of an electron) to $\sim 5 m_0$ by Pb^{2+} doping, indicating the dramatic change of the DOS (details later).¹¹² The electronic structure analysis provided an explanation for the carrier mobility (μ) enhancement, as summarized below. However, it may partly result from the grain texturation as some preferential orientation could be observed in the XRD pattern. As shown in the **Fig. 14(a)**, the normalized mobility $\mu(m^*)^{3/2}$ of the Pb^{2+} doped sample is higher than those obtained with M^{2+} ($\text{M} = \text{Mg}, \text{Sr}, \text{and Ba}$) doped ones. The increased normalized mobility $\mu(m^*)^{3/2}$ and reduced thermal conductivity lead to a maximum ZT of 1.14 at 823 K in 0.06 Pb doped BiCuSeO , as shown in **Fig. 14(b)**.

Fig. 14(c) depicts the electronic structure calculation in details, which shows that the enhancement of the hole mobility is very likely due to the Pb-induced delocalized lone-pair $6s$ orbitals in the electronic states close to valence-band maximum, which are primarily responsible for hole transport.¹¹² By using first-principles calculations, Pb substitution for a Bi atom (compared with other dopants, such as Mg, Sr, and Ba) gives the lowest defect formation energy in $\text{Bi}_{0.875}\text{M}_{0.125}\text{CuSeO}$ ($\text{M} = \text{Pb}, \text{Mg}, \text{Sr}, \text{and Ba}$) among all possible configurations. In addition, on the basis of the relaxed $\text{Bi}_{0.875}\text{M}_{0.125}\text{CuSeO}$ structures with the substitution impurity M^{2+} , the orbital-projected DOS and orbital-projected band structures were calculated use $2 \times 2 \times 1$ supercell and

a composition $\text{Bi}_{0.875}\text{Pb}_{0.125}\text{CuSeO}$. As aforementioned, it is similar to the case of $\text{BiCu}_{1-x}\text{SeO}$ calculation, the selected small $2 \times 2 \times 1$ supercell may be caused calculation uncertainty. The authors reported that Pb^{2+} doping introduces substantial 6s components into the states close to the valence band maximum, while the *s* states from Mg, Sr, and Ba only contribute deep in the conduction band. Such delocalized 6s orbitals from the lone pair electrons in Pb are believed to be helpful to enhance the hole mobility. Thus, the Pb doping would enhance the electrical conductivity more effectively than other dopants.

Pan *et al.* observed somewhat distinct results of both carrier mobility and electronic structure in BiCuSeO upon Pb^{2+} doping.¹³² As shown in **Fig. 14(d)**, the carriers mobility decreases with increasing Pb doping level, which is contrary to what Lan *et al.* reported.¹¹² Regarding the electronic structure, both Pan *et al.* and Barreteau *et al.* did not find any DOS distortions in BiCuSeO due to Pb doping, which was supposed to be responsible for the enhanced the effective mass.^{99, 132} As shown in the **Fig. 14(e)**, the Seebeck coefficient of Sr doped samples is similar to that of Pb doped ones, invoking us to evaluate the effects on the band structure of BiCuSeO with different doping elements. Specifically, the Sommerfeld coefficient (γ) was measured to estimate the DOS at the Fermi level $D(E_F)$ for both spin directions according to:^{99, 132}

$$\gamma = \frac{\pi^2 k_B^2}{3} D(E_F) (1 + \lambda_{e-ph}) \quad (7)$$

where λ_{e-ph} is the electron-phonon coupling constant, which was set to zero. The magnitude of $D(E_F)$ of Pb doped samples increased monotonically with increasing Pb content, as shown in **Fig. 14(e)**. This observation was consistent with the $\text{Bi}_{1-x}\text{Sr}_x\text{CuSeO}$ series, in which the density of states increased up to $\text{Sr} = 0.2$ where it started to decrease, in agreement with the band structure calculations. Thus, a similar $D(E_F)$ for both Pb and Sr doped samples was observed. This measured DOS at Fermi level for Pb and Sr doped samples using the Sommerfeld coefficient would indicate that the DOS is exactly the same for Pb^{2+} and Sr^{2+} at fixed carriers concentration, which would means that the Pb^{2+} has slight effect on the electronic structure of

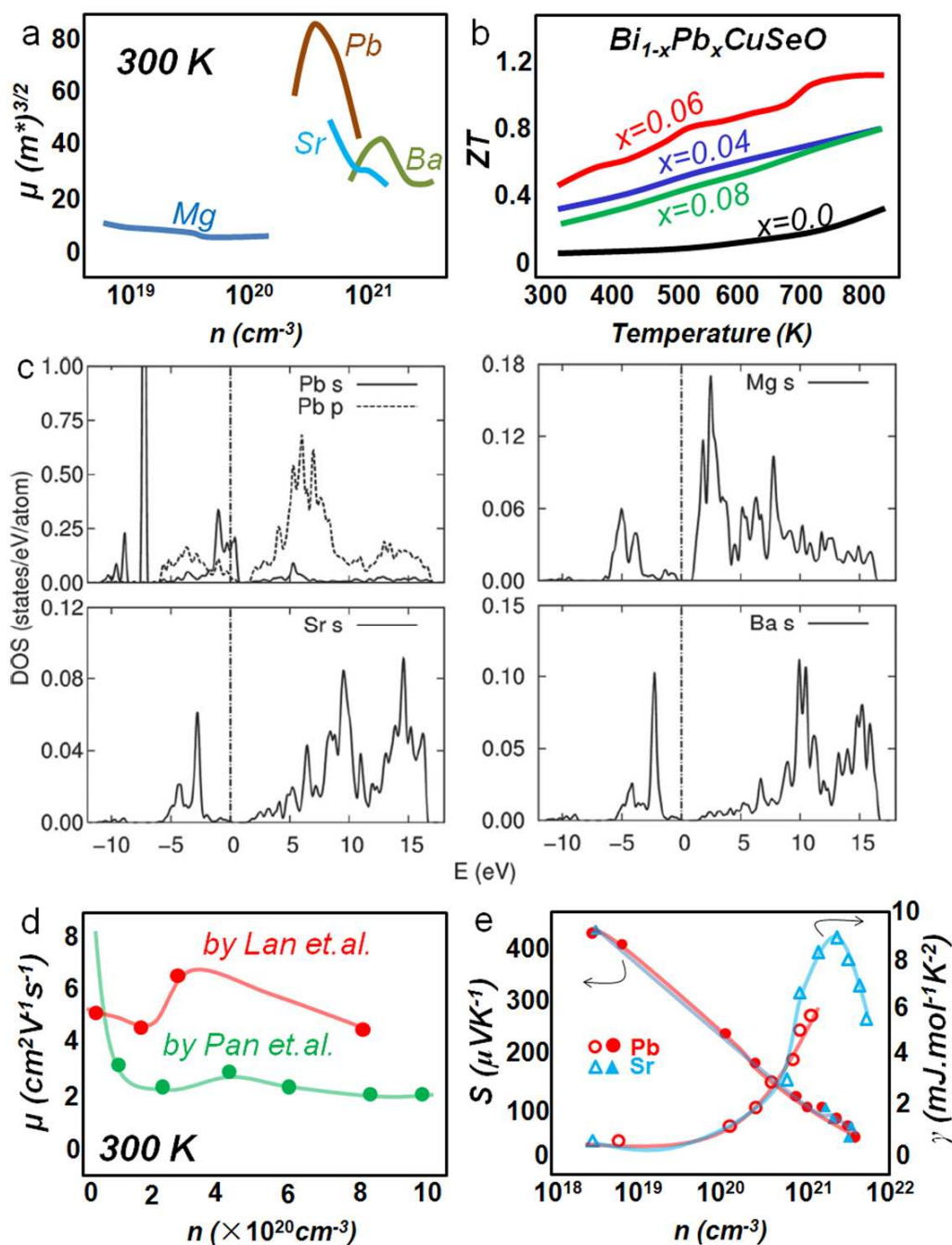
BiCuSeO.^{99, 132}

Fig. 14 (a) Carriers concentration dependence of normalized mobility in $\text{Bi}_{0.875}\text{M}_{0.125}\text{CuSeO}$ [$M = \text{Pb}, \text{Mg}, \text{Sr}, \text{and Ba}$] systems. (b) Dimensionless figure-of-merit ZT of the $\text{Bi}_{1-x}\text{Pb}_x\text{CuSeO}$. (c) Orbital-projected density of states in $\text{Bi}_{0.875}\text{M}_{0.125}\text{CuSeO}$.^{26, 27, 30, 112} It is clear that only Pb 6s electrons significantly contribute to the states close to the valence band maximum (VBM) responsible for hole transport. (d) Carriers mobility as a function of carriers concentration for Pb doped BiCuSeO. (e) Seebeck coefficient and Sommerfeld coefficient as a function of carriers concentration modified by Pb and Sr doping. Reproduced with permission from ref. 112. Copyright 2013 Wiley.

Despite that interesting physical and chemical behaviors were observed in Pb doped BiCuSeO, the underlying mechanisms still need further clarifications. For example, one can speculate that the observed nanoinclusions might contribute to the thermal conductivity reduction and ZT enhancement, as a long-time perspective, further evidences shall be gathered through performing HRTEM on these nanostructures.

Improving performance through band gaps tuning:

A low electrical conductivity of the pristine BiCuSeO mainly results from its relatively narrow band gap ~ 0.8 eV, while an even narrower band gap of 0.4 eV was reported in its analogue BiCuTeO by Hiramatsu *et.al.*⁹⁵ Later on, a solid solution study of BiCuSeO/BiCuTeO was reported by Barreteau *et.al.*,¹²⁵ who found that Te substitution of Se has a significantly influence on the structural and electronic properties of BiCuSeO, and that a complete solid solution exists between the two end members BiCuSeO and BiCuTeO. Here, we introduce that an improved thermoelectric performance can be achieved by substituting Te on Se site in $(\text{Cu}_2\text{Se}_2)^{2-}$ layers, as reported by Liu *et al.*²⁸ A smaller band gap also implies a smaller resistivity but also a smaller Seebeck coefficient, therefore, a good balance between two sides could result in an optimal power factor. Indeed, a ZT of 0.71 at 923K was achieved in BiCuSe_{0.94}Te_{0.06}O, and this value is nearly 1.5 times larger than that of pristine BiCuSeO.

The proposed mechanism is schematically illustrated in **Fig. 15(a)**. As band gap decreases, a growing number of electrons can be excited across the band gap into the conduction band, leaving same quantity of holes in the valence band, eventually resulting in a promoted electrical conductivity. Experimental evidence of shrinking band gap due to Te replacing Se in BiCuSeO is provided in **Fig. 15(b)**, where the electronic absorption spectra of BiCuSe_{1-x}Te_xO. The absorption edge shifts towards lower energy with increasing Te fraction, and the band gap shows a systematic reduction with increasing Te fraction x , from ~ 0.8 eV to ~ 0.65 eV in going from $x = 0$ to 0.2.²⁸

The temperature dependence of the electrical conductivity of $\text{BiCuSe}_{1-x}\text{Te}_x\text{O}$ is shown in **Fig. 15(c)**.²⁸ All the curves increase with elevating temperature, showing semiconducting behaviors. The change on electrical conductivity with increasing Te fraction at room temperature is negligible, probably due to neutral impurity scattering of the charge carriers. However, the electrical conductivity shows a significant improvement above from 550 K, and reaches to $\sim 40 \text{ Scm}^{-1}$ at 923 K for $\text{BiCuSe}_{0.85}\text{Te}_{0.15}\text{O}$, which is much larger than pristine BiCuSeO ($\sim 15 \text{ Scm}^{-1}$) at the same temperature. The enhancement of electrical conductivity at high temperature can be attributed to the onset of thermal excitation of electrons across the band gap into the conduction band at $\sim 550 \text{ K}$. Coupled with low thermal conductivity values, the optimized power factor contributes to a ZT of 0.71 at 923 K in $\text{BiCuSe}_{0.94}\text{Te}_{0.06}\text{O}$, as shown in **Fig. 15(d)**.²⁸ This is a successful route to improve the thermoelectric performances by tuning the band gap of BiCuSeO system through Te substitution on Se site.

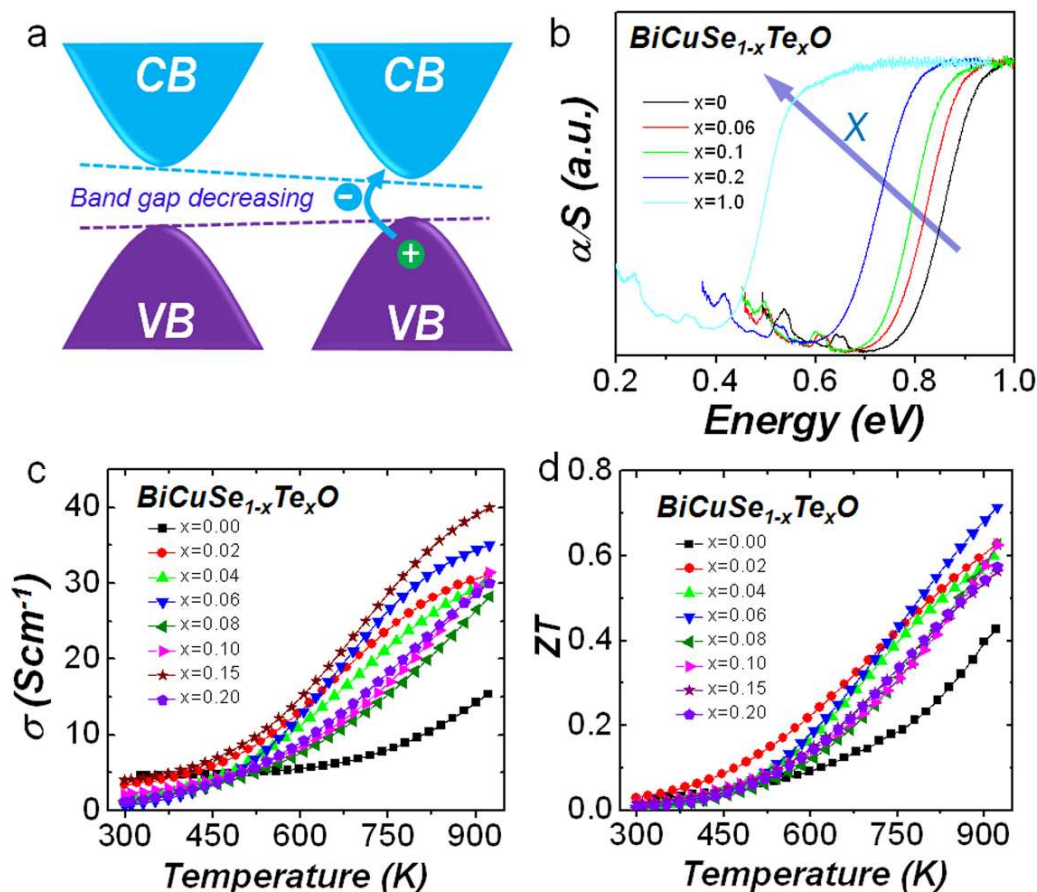


Fig. 15 (a) The schematic figure for band gap tuning, CB: conduction band, VB: valence band. (b) Electronic absorption spectra of $\text{BiCuSe}_{1-x}\text{Te}_x\text{O}$. (c) Electrical conductivity depends of temperature. (d) Dimensionless figure-of-merit ZT depends of temperature. Ref. 28, reproduced by permission of The Royal Society of Chemistry.

Increasing mobility and performance through samples texturation:

The low carrier mobility $\sim 22 \text{ cm}^2\text{V}^{-1}\text{s}^{-1}$ at room temperature is the bottleneck for pristine BiCuSeO , greatly limits the improvement of the electrical transport properties and its thermoelectric performance, and even worse, since most of previous studies focused on the carriers concentration enhancement through various doping, the carriers mobility was further deteriorated due to impurity scattering, even down to $1 \sim 2 \text{ cm}^2\text{V}^{-1}\text{s}^{-1}$ as the carriers concentration increases up to order of $1 \times 10^{21} \text{ cm}^{-3}$. As BiCuSeO oxyselenides crystallize in a layered structure, the electrical and thermal transport in BiCuSeO system should be anisotropic in single crystal, and a higher in-plane carriers mobility could be expected. Moreover, in polycrystalline bulk, this intrinsic layered structure leads to the formation of platelet grains, with a preferential orientation due to extrinsic forces, a strong anisotropy of the grain boundaries concentration can be achieved between the c -axis and in-plan direction. This anisotropy (either intrinsic or extrinsic) can be well utilized to improve the carrier mobility.

Sui *et al.* applied hot-forging processes to obtain textured samples, where a - b plane of the grains were preferentially oriented perpendicular to the pressing direction through samples deformation under external applied pressure (hot-forging), as depicted in **Fig. 16(a)**. The start-up pellets were synthesized by a conventional two-step solid state reaction route, and the highly textured samples were realized by repeating hot forging processes through the sample deformation within an extra space in a bigger mold.⁷³

The highly textured microstructures after hot-forging processes were confirmed under scanning electron microscopy (SEM) with electron backscattering diffraction (EBSD) detector. It is shown in **Fig. 16(b)** that the platelet grains are oriented perpendicular to the pressing direction of $\text{Bi}_{0.875}\text{Ba}_{0.125}\text{CuSeO}$. The grains with red,

green and blue color are oriented along [001], [010] and [110] directions, respectively. With increasing the number of the hot-forging steps, the grains experience slight growth, but the preferential grains orientation along the [001] direction (red color grains) is more and more obvious. The pole figures on the right clearly reflect that the orientation of grains changes from absolute disorder before hot-forging to [001] direction after hot-forging.⁷³

Fig. 16(c) indicates that the carriers concentration was not influenced by the hot-forging processes, while that the carriers mobility was increased from $2 \text{ cm}^2\text{V}^{-1}\text{s}^{-1}$ in the sample without hot-forging to $\sim 3 \text{ cm}^2\text{V}^{-1}\text{s}^{-1}$, $\sim 3.7 \text{ cm}^2\text{V}^{-1}\text{s}^{-1}$ and $\sim 4.2 \text{ cm}^2\text{V}^{-1}\text{s}^{-1}$ after one, two and three hot-forging steps, respectively. The grains orientation could also lead to an increase of the lattice thermal conductivity in the perpendicular direction, which might weaken the benefit from the enhanced electrical conductivity. As can be seen in **Fig. 16(d)**, the ratio of electrical to thermal conductivity was enhanced in the direction perpendicular to the pressing, but impaired in the direction parallel to the pressing. After the hot-forging processes, the ZT measured in the direction parallel to the pressing was reduced, yet improved from ~ 1.1 to ~ 1.4 at 923 K in the perpendicular direction after three hot-forging steps, **Fig. 16(e)**. This is a record ZT value in the BiCuSeO system, indicating that texturation is a promising technique to effectively improve the thermoelectric performance in the BiCuSeO system. The ZT of 1.4 at 923 K makes BiCuSeO a robust candidate for medium temperature thermoelectric applications.⁷³

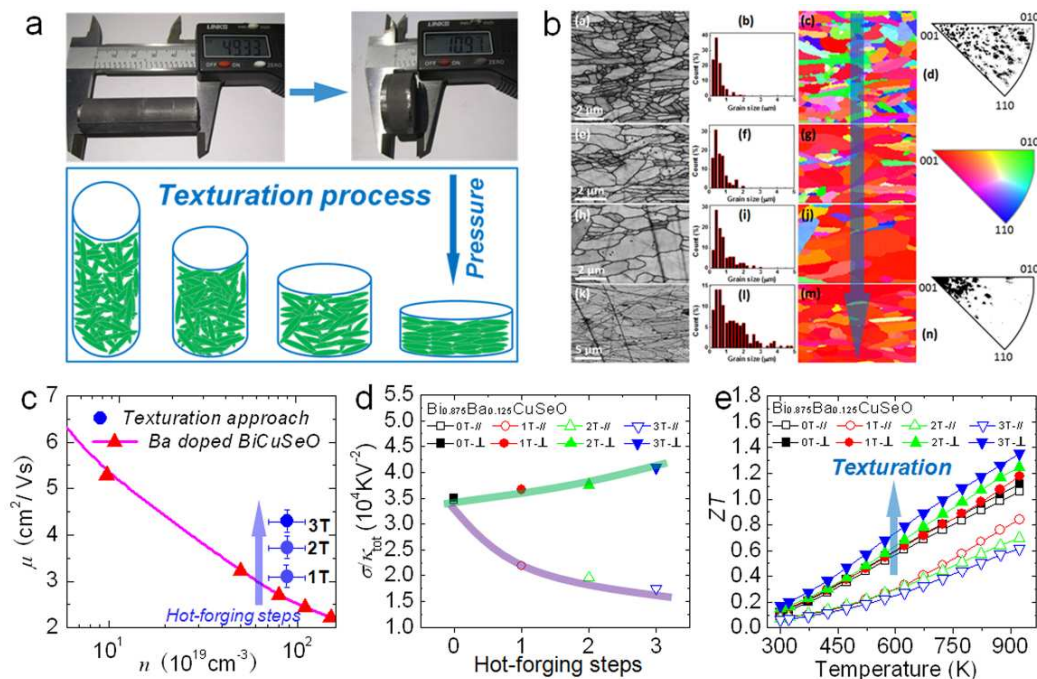


Fig. 16 (a) Typical samples used in this study from as-synthesized sample (0T) to 3 steps hot-forged sample (3T), and the scheme of hot-forging process. (b) EBSD microstructures, grain size distribution histograms, and inverse pole figures of textured Bi_{0.875}Ba_{0.125}CuSeO from as-synthesized sample (0T) to 3 steps hot-forged sample (3T). (c) Room temperature carrier mobility of textured Bi_{0.875}Ba_{0.125}CuSeO and Bi_{1-x}Ba_xCuSeO with similar carrier concentrations are plotted for comparison. (d) The ratio of electrical to thermal conductivity as a function of the number of hot-forging steps. (e) Figure of merit ZT of textured Bi_{0.875}Ba_{0.125}CuSeO. Ref. 73, reproduced by permission of The Royal Society of Chemistry.

5. Theoretical calculations of the thermoelectric properties of BiCuSeO

Theoretical calculations of thermoelectric properties were utilized to provide support and guide to experiments. Zou *et al.* calculated the thermoelectric properties of BiCuSeO with different doping levels on the Bi site, and estimated the optimal doping concentration to predict a maximum thermoelectric performance.¹³³ The calculations of electronic transport properties were based on semi-classical Boltzmann transport equation (BTE) in conjunction with rigid band approximation, showing good agreement with experimental data. In this calculation, an energy-independent constant relaxation time approximation was adopted, and the influence of the bands' non-parabolicity on the relaxation time was neglected since it was difficult to derive the

relaxation time from *ab initio* band calculations.

The calculated thermoelectric properties of BiCuSeO as a function of temperature are shown in **Fig. 17**. As seen in **Fig. 17(a)**, the Seebeck coefficient increases monotonously with temperature over the whole range. At a given temperature, the Seebeck coefficient decreases as the doping level increases. The calculated Seebeck coefficient of BiCuSeO agrees well with the experimental data especially above 500 K. The calculated electrical conductivities are shown in **Fig. 17(b)**. The results show that the electrical conductivity decreases with temperature and exhibits a metal-like behavior. Furthermore, the electrical conductivity at a given temperature increases with increasing doping level. It is noteworthy that the deviation of theoretical calculations from experimental observations in the low temperature regime could be ascribed to the over-simplified constant relaxation time approximation.¹³³

To obtain the total thermal conductivity, the lattice thermal conductivity was assumed to obey a $1/T$ Umklapp phonon scattering behavior to fit the experimental data, and the electronic thermal conductivity was given by the Wiedemann-Franz law. The fitted thermal conductivity is plotted in **Fig. 17(c)**, and matches well with the experimental data. It is seen that the total thermal conductivity decreases with climbing temperature, and increases with elevated carriers concentration.¹³³

With the calculated electrical and thermal transport properties, the figure of merit ZT of *p*-type BiCuSeO can be obtained as a function of temperature, as shown in **Fig. 17(d)**. The calculations confirm the experimental observations that ZT can be enhanced in the high temperature range (above 600 K) *via* optimizing doping level. Theoretically, ZT shows an increasing trend with temperature, and a maximum value of 1.32 is predicted at 1000 K for the 12.5% (elements doping level on the Bi site) doped BiCuSeO.¹³³ The slightly higher theoretical values come partially from the overestimated electrical conductivity values.

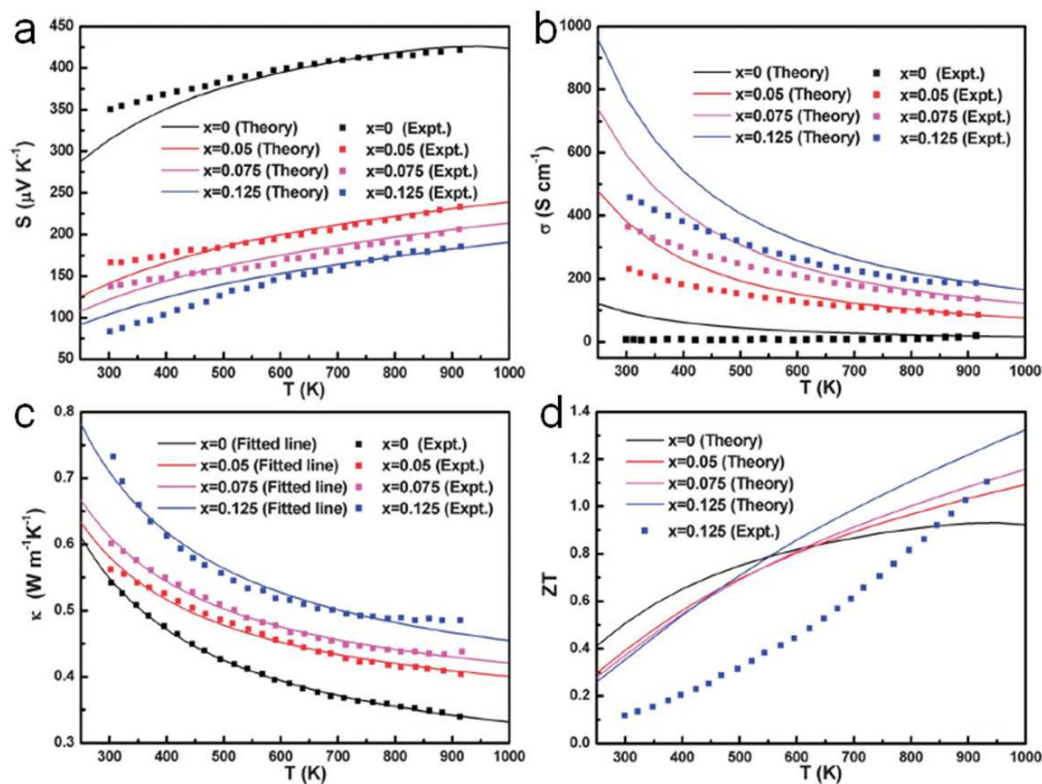


Fig. 17 Calculated thermoelectric properties of BiCuSeO as a function of temperature, x is the doping level on the Bi site; (a) Seebeck coefficient. (b) Electrical conductivity. (c) Total thermal conductivity, and (d) Dimensionless figure-of-merit ZT . In the figure, the experimental data from the reference,²⁷ x is the number of holes in BiCuSeO. Reproduced from ref. 133 with permission from The Royal Society of Chemistry.

6. Summary and outlook

In this perspective, we have reviewed and summarized the crystal structure, microstructure, electronic structure and physical/chemical properties of BiCuSeO oxyselenides, which have been reported as very promising thermoelectric materials since 2010. To date, BiCuSeO oxyselenides have received ever-increasing attention and have been extensively studied, and the thermoelectric performance ZT was significantly increased from 0.5 for pristine BiCuSeO to 1.4 by texturation of optimally doped materials. The intrinsically low thermal conductivity of BiCuSeO implies that the most effective method to enhance ZT via enhancing the electrical transport properties. In the past three years, many effective approaches were successfully applied in BiCuSeO systems, which include optimizing carriers concentration through doping,

band gap tuning, and increasing carrier mobility through texturing. If these power factor enhancing approaches were combined together to achieve a synergistic approach, they would probably further improve the performance of these BiCuSeO materials. Despite vast efforts on BiCuSeO oxyselenides were devoted, the researches on the oxyselenides family as promising thermoelectrics are still at a relatively infant stage, and thus many fundamental and technical issues remain to be further investigated, which at least include:

(1) Novel synergistic approaches need to be developed to further enhance the power factor yet maintain the low thermal conductivity. Currently several possibilities might be suggestive. For instance, the much anticipated technique of implanting resonance states to increase the Seebeck coefficient and the overall power factor has not yet been realized in BiCuSeO systems. In addition, the effective band convergence in enhancing the Seebeck coefficient in PbTe⁵ and Mg₂Si⁶ systems, can be expected to extend to *p*-type BiCuSeO systems. Since a high carrier mobility exists in the in-plane direction of the layered structure for BiCuSeO, it can be expected that the carrier mobility in BiCuSeO single crystals will be much higher than that of 22 cm²V⁻¹s⁻¹ in BiCuSeO polycrystalline, and possibly a high *ZT* of 2.0 can be achieved in BiCuSeO single crystals. However, the single crystal growth in BiCuSeO system is extremely challenging with current synthesis technologies.

(2) BiCuSeO belongs to the more general family of *LnCuChO* (*Ln* = lanthanide, *Ch* = S, Se, Te), thus many analogues are worthy exploring, examples include BiCuTeO,¹⁰⁹ BiCuSO, LaCuSeO, CeCuSeO, *etc.*

(3) Since BiCuSeO has high *ZT* value over 1, but it is still *p*-type thermoelectric. Therefore, *n*-type compound based on BiCuSeO system with high *ZT* value is more urgent. Extensively studied are warranted in *n*-type compounds with layered ZrCuSiAs structures, such as respectively doped in Bi and Cu sites by elements with positive valence >3 and >1, or doped in Se and O sites by elements with negative charge of -1.

(4) Besides the improvement of the thermoelectric performance, studies should be devoted to assess and understand the electrode materials, the contact resistivity,

thermal stability for the high performance and the mechanical properties. These mentioned above are also critical for thermoelectric device fabrication. Understanding mechanical robustness issues in the new high performance materials will help open the path to device assembly, testing and ultimately commercialization.

Acknowledgements

This work was supported by the Triangle de la Physique under Project No. STP 2008-095T, by the International Cooperation Department of Université Paris-Sud XI, by the ANR through the project OTHer (ANR 2011 JS08 012 01) and NSFC under grant No. 51221291 (Y.H.L., J.F.L. and C.W.N.). This contribution was partly supported by the startup of South University of Science and Technology of China from Shenzhen government and national 1000 plan for young scientists (J.Q.H). The authors (L.D.Z. and J.Q.H) are grateful to Professor Mercouri G. Kanatzidis for helpful discussions. We also thank Professors W. Cai, J. H. Sui, Y. L. Pei, E. Amzallag, Y. Liu, and W. Xu for plentiful discussions and fruitful collaborations. Of course most of all, we are grateful to the numerous dedicated graduate students and postdoctoral fellows who have contributed to our thermoelectric research efforts. Their names appear in the various publications cited in this article.

References

1. L. D. Zhao, V. P. Dravid and M. G. Kanatzidis, *Energy Environ. Sci.*, 2014, **7**, 251-268.
2. G. A. Slack and V. G. Tsoukala, *J. Appl. Phys.*, 1994, **76**, 1665-1671.
3. J. P. Heremans, V. Jovovic, E. S. Toberer, A. Saramat, K. Kurosaki, A. Charoenphakdee, S. Yamanaka and G. J. Snyder, *Science*, 2008, **321**, 554-557.
4. J. P. Heremans, B. Wiendlocha and A. M. Chamoire, *Energy Environ. Sci.*, 2012, **5**, 5510-5530.
5. Y. Z. Pei, X. Y. Shi, A. LaLonde, H. Wang, L. D. Chen and G. J. Snyder, *Nature*, 2011, **473**, 66-69.
6. W. Liu, X. J. Tan, K. Yin, H. J. Liu, X. F. Tang, J. Shi, Q. J. Zhang and C. Uher, *Phys. Rev. Lett.*, 2012, **108**, 166601.
7. L. D. Hicks, T. C. Harman, X. Sun and M. S. Dresselhaus, *Phys. Rev. B*, 1996, **53**, 10493-10496.
8. J. P. Heremans, C. M. Thrush and D. T. Morelli, *Phys. Rev. B*, 2004, **70**, 115334.

9. K. F. Hsu, S. Loo, F. Guo, W. Chen, J. S. Dyck, C. Uher, T. Hogan, E. K. Polychroniadis and M. G. Kanatzidis, *Science*, 2004, **303**, 818-821.
10. M. Zhou, J. F. Li and T. Kita, *J. Am. Chem. Soc.*, 2008, **130**, 4527-4532.
11. J. H. Li, Q. Tan, J. F. Li, D. W. Liu, F. Li, Z. Y. Li, M. M. Zou and K. Wang, *Adv. Func. Mater.*, 2013, **23**, 4317-4323.
12. J. R. Sootsman, D. Y. Chung and M. G. Kanatzidis, *Angew. Chem.-Int. Edit.*, 2009, **48**, 8616-8639.
13. J.-F. Li, W.-S. Liu, L.-D. Zhao and M. Zhou, *NPG Asia Mater.*, 2010, **2**, 152-158.
14. M. G. Kanatzidis, *Chem. Mater.*, 2010, **22**, 648-659.
15. M. S. Dresselhaus, G. Chen, M. Y. Tang, R. G. Yang, H. Lee, D. Z. Wang, Z. F. Ren, J. P. Fleurial and P. Gogna, *Adv. Mater.*, 2007, **19**, 1043-1053.
16. K. Biswas, J. He, I. D. Blum, C. I. Wu, T. P. Hogan, D. N. Seidman, V. P. Dravid and M. G. Kanatzidis, *Nature*, 2012, **489**, 414-418.
17. J. Q. He, M. G. Kanatzidis and V. P. Dravid, *Mater. Today*, 2013, **16**, 166-176.
18. L. D. Zhao, S. Q. Hao, S. H. Lo, C. I. Wu, X. Y. Zhou, Y. Lee, H. Li, K. Biswas, T. P. Hogan, C. Uher, C. Wolverton, V. P. Dravid and M. G. Kanatzidis, *J. Am. Chem. Soc.*, 2013, **135**, 7364-7370.
19. L. D. Zhao, J. Q. He, S. Q. Hao, C. I. Wu, T. P. Hogan, C. Wolverton, V. P. Dravid and M. G. Kanatzidis, *J. Am. Chem. Soc.*, 2012, **134**, 16327-16336.
20. L. D. Zhao, S. H. Lo, Y. S. Zhang, H. Sun, G. J. Tan, C. Uher, C. Wolverton, V. P. Dravid, M. G. Kanatzidis, *Nature* **2014**, **508**, 373-377.
21. M. D. Nielsen, V. Ozolins and J. P. Heremans, *Energy Environ. Sci.*, 2013, **6**, 570-578.
22. (a) H. Wang, J. F. Li, M. M. Zou and T. Sui, *Appl. Phys. Lett.*, 2008, **93**, 202106.; (b) D. T. Morelli, V. Jovic and J. P. Heremans, *Phys. Rev. Lett.*, 2008, **101**, 035901.
23. S. R. Brown, S. M. Kauzlarich, F. Gascoin and G. J. Snyder, *Chem. Mater.*, 2006, **18**, 1873-1877.
24. K. Kurosaki, A. Kosuga, H. Muta, M. Uno and S. Yamanaka, *Appl. Phys. Lett.*, 2005, **87**, 061919.
25. J. S. Rhyee, K. H. Lee, S. M. Lee, E. Cho, S. Il Kim, E. Lee, Y. S. Kwon, J. H. Shim and G. Kotliar, *Nature*, 2009, **459**, 965-968.
26. J. Li, J. H. Sui, C. Barreateau, D. Berardan, N. Dragoe, W. Cai, Y. L. Pei and L. D. Zhao, *J. Alloys Compd.*, 2013, **551**, 649-653.
27. J. Li, J. H. Sui, Y. L. Pei, C. Barreateau, D. Berardan, N. Dragoe, W. Cai, J. Q. He and L. D. Zhao, *Energy Environ. Sci.*, 2012, **5**, 8543-8547.
28. Y. Liu, J. L. Lan, W. Xu, Y. C. Liu, Y. L. Pei, B. Cheng, D. B. Liu, Y. H. Lin and L. D. Zhao, *Chem. Commun.*, 2013, **49**, 8075-8077.
29. Y. L. Pei, J. Q. He, J. F. Li, F. Li, Q. J. Liu, W. Pan, C. Barreateau, D. Berardan, N. Dragoe and L. D. Zhao, *NPG Asia Mater.*, 2013, **5**, e47.
30. L. D. Zhao, D. Berardan, Y. L. Pei, C. Byl, L. Pinsard-Gaudart and N. Dragoe, *Appl. Phys. Lett.*, 2010, **97**, 092118.
31. F. Li, T. R. Wei, F. Y. Kang and J. F. Li, *J. Mater. Chem. A*, 2013, **1**, 11942-11949.
32. G. J. Snyder and E. S. Toberer, *Nat. Mater.*, 2008, **7**, 105-114.
33. D. Y. Chung, T. Hogan, P. Brazis, M. Rocci-Lane, C. Kannewurf, M. Bastea, C. Uher and M. G. Kanatzidis, *Science*, 2000, **287**, 1024-1027.

34. B. Poudel, Q. Hao, Y. Ma, Y. C. Lan, A. Minnich, B. Yu, X. A. Yan, D. Z. Wang, A. Muto, D. Vashaee, X. Y. Chen, J. M. Liu, M. S. Dresselhaus, G. Chen and Z. F. Ren, *Science*, 2008, **320**, 634-638.
35. W.-S. Liu, Q. Zhang, Y. Lan, S. Chen, X. Yan, Q. Zhang, H. Wang, D. Wang, G. Chen and Z. Ren, *Adv. Energy Mater.*, 2011, **1**, 577-587.
36. W. Liu, K. C. Lukas, K. McEnaney, S. Lee, Q. Zhang, C. P. Opeil, G. Chen and Z. Ren, *Energy Environ. Sci.*, 2013, **6**, 552-560.
37. X. B. Zhao, X. H. Ji, Y. H. Zhang, T. J. Zhu, J. P. Tu and X. B. Zhang, *Appl. Phys. Lett.*, 2005, **86**, 062111.
38. L. D. Zhao, B. P. Zhang, W. S. Liu and J. F. Li, *J. Appl. Phys.*, 2009, **105**, 023704-023706.
39. L. D. Zhao, J. Q. He, C. I. Wu, T. P. Hogan, X. Y. Zhou, C. Uher, V. P. Dravid and M. G. Kanatzidis, *J. Am. Chem. Soc.*, 2012, **134**, 7902-7912.
40. Q. Zhang, F. Cao, W. Liu, K. Lukas, B. Yu, S. Chen, C. Opeil, D. Broido, G. Chen and Z. Ren, *J. Am. Chem. Soc.*, 2012, **134**, 10031-10038.
41. Q. Zhang, F. Cao, K. Lukas, W. Liu, K. Esfarjani, C. Opeil, D. Broido, D. Parker, D. J. Singh, G. Chen and Z. Ren, *J. Am. Chem. Soc.*, 2012, **134**, 17731-17738.
42. Q. Zhang, Y. Lan, S. Yang, F. Cao, M. Yao, C. Opeil, D. Broido, G. Chen and Z. Ren, *Nano Energy*, 2013, **2**, 1121-1127.
43. Z. Du, J. Cui, T. Zhu and X. Zhao, *Phys. Status Solidi A*, 2013, **210**, 2359-2363.
44. X. Liu, T. Zhu, H. Wang, L. Hu, H. Xie, G. Jiang, G. J. Snyder and X. Zhao, *Adv. Energy Mater.*, 2013, **3**, 1238-1244.
45. G. Tan, W. Liu, H. Chi, X. Su, S. Wang, Y. Yan, X. Tang, W. Wong-Ng and C. Uher, *Acta Mater.*, 2013, **61**, 7693-7704.
46. G. Tan, W. Liu, S. Wang, Y. Yan, H. Li, X. Tang and C. Uher, *J. Mater. Chem. A*, 2013, **1**, 12657-12668.
47. G. Tan, Y. Zheng and X. Tang, *Appl. Phys. Lett.*, 2013, **103**, 183904.
48. X. Shi, J. Yang, J. R. Salvador, M. Chi, J. Y. Cho, H. Wang, S. Bai, J. Yang, W. Zhang and L. Chen, *J. Am. Chem. Soc.*, 2011, **133**, 7837-7846.
49. W. S. Liu, B. P. Zhang, J. F. Li, H. L. Zhang and L. D. Zhao, *J. Appl. Phys.*, 2007, **102**, 103717.
50. W. S. Liu, B. P. Zhang, L. D. Zhao and J. F. Li, *Chem. Mater.*, 2008, **20**, 7526-7531.
51. H. Xie, H. Wang, Y. Pei, C. Fu, X. Liu, G. J. Snyder, X. Zhao and T. Zhu, *Adv. Func. Mater.*, 2013, **23**, 5123-5130.
52. H. Lin, L. A. Wray, Y. Xia, S. Xu, S. Jia, R. J. Cava, A. Bansil and M. Z. Hasan, *Nat. Mater.*, 2010, **9**, 546-549.
53. S. Sakurada and N. Shutoh, *Appl. Phys. Lett.*, 2005, **86**, 103717.
54. Q. Shen, L. Chen, T. Goto, T. Hirai, J. Yang, G. P. Meisner and C. Uher, *Appl. Phys. Lett.*, 2001, **79**, 4165-4167.
55. C. Uher, J. Yang, S. Hu, D. T. Morelli and G. P. Meisner, *Phys. Rev. B*, 1999, **59**, 8615-8621.
56. V. L. Kuznetsov, L. A. Kuznetsova, A. E. Kaliazin and D. M. Rowe, *J. Appl. Phys.*, 2000, **87**, 7871-7875.
57. G. K. H. Madsen, K. Schwarz, P. Blaha and D. J. Singh, *Phys. Rev. B*, 2003, **68**, 125212-125217.
58. G. S. Nolas, J. L. Cohn, G. A. Slack and S. B. Schujman, *Appl. Phys. Lett.*, 1998, **73**, 178-180.

59. G. S. Nolas, T. J. R. Weakley, J. L. Cohn and R. Sharma, *Phys. Rev. B*, 2000, **61**, 3845-3850.
60. G. Joshi, H. Lee, Y. C. Lan, X. W. Wang, G. H. Zhu, D. Z. Wang, R. W. Gould, D. C. Cuff, M. Y. Tang, M. S. Dresselhaus, G. Chen and Z. F. Ren, *Nano Lett.*, 2008, **8**, 4670-4674.
61. N. Mingo, D. Hauser, N. P. Kobayashi, M. Plissonnier and A. Shakouri, *Nano Lett.*, 2009, **9**, 711-715.
62. X. W. Wang, H. Lee, Y. C. Lan, G. H. Zhu, G. Joshi, D. Z. Wang, J. Yang, A. J. Muto, M. Y. Tang, J. Klatsky, S. Song, M. S. Dresselhaus, G. Chen and Z. F. Ren, *Appl. Phys. Lett.*, 2008, **93**, 193121.
63. F. Gascoin, S. Ottensmann, D. Stark, S. M. Haile and G. J. Snyder, *Adv. Func. Mater.*, 2005, **15**, 1860-1864.
64. E. S. Toberer, C. A. Cox, S. R. Brown, T. Ikeda, A. F. May, S. M. Kauzlarich and G. J. Snyder, *Adv. Func. Mater.*, 2008, **18**, 2795-2800.
65. E. S. Toberer, A. F. May and G. J. Snyder, *Chem. Mater.*, 2010, **22**, 624-634.
66. K. Koumoto, R. Funahashi, E. Guilmeau, Y. Miyazaki, A. Weidenkaff, Y. F. Wang and C. L. Wan, *J. Am. Ceram. Soc.*, 2013, **96**, 1-23.
67. E. M. Levin, S. L. Bud'ko and K. Schmidt-Rohr, *Adv. Func. Mater.*, 2012, **22**, 2766-2774.
68. J. P. Fleurial, T. Caillat and A. Borshchevsky, in *Thirteenth International Conference on Thermoelectrics*, eds. B. Mathiprakasam and P. Heenan, Aip Press, Woodbury, 1995, pp. 40-44.
69. S. Bobev, V. Fritsch, J. D. Thompson, J. L. Sarrao, B. Eck, R. Dronskowski and S. M. Kauzlarich, *J. Solid State Chem.*, 2005, **178**, 1071-1079.
70. D. M. Young and S. M. Kauzlarich, *Chem. Mater.*, 1995, **7**, 206-209.
71. A. F. May, E. S. Toberer and G. J. Snyder, *J. Appl. Phys.*, 2009, **106**, 013706.
72. X. Yan, W. S. Liu, H. Wang, S. Chen, J. Shiomi, K. Esfarjani, H. Z. Wang, D. Z. Wang, G. Chen and Z. F. Ren, *Energy Environ. Sci.*, 2012, **5**, 7543-7548.
73. J. H. Sui, J. Li, J. Q. He, Y. L. Pei, D. Berardan, H. J. Wu, N. Dragoe, W. Cai and L. D. Zhao, *Energy Environ. Sci.*, 2013, **6**, 2916-2920.
74. M. Palazzi, C. Carcaly and J. Flahaut, *J. Solid State Chem.*, 1980, **35**, 150-155.
75. M. Palazzi and S. Jaulmes, *Acta Crystallogr. B*, 1981, **37**, 1337-1339.
76. T. Ohtani, M. Hirose, T. Sato, K. Nagaoka and M. Iwabe, *Jpn. J. Appl. Phys.*, 1993, **32**, 316-318.
77. K. Sekizawa, Y. Takano, K. Mori and K. Yahagi, *Czechoslovak J. Phys.*, 1996, **46**, 1943-1944.
78. Y. Takano, C. Ogawa, Y. Miyahara, H. Ozaki and K. Sekizawa, *J. Alloys Compd.*, 1997, **249**, 221-223.
79. K. Ishikawa, S. Kinoshita, Y. Suzuki, S. Matsuura, T. Nakanishi, M. Aizawa and Y. Suzuki, *Journal of the Electrochemical Society*, 1991, **138**, 1166-1170.
80. P. S. Berdonosov, A. M. Kusainova, L. N. Kholodkovskaya, V. A. Dolgikh, L. G. Akselrud and B. A. Popovkin, *J. Solid State Chem.*, 1995, **118**, 74-77.
81. A. M. Kusainova, P. S. Berdonosov, L. G. Akselrud, L. N. Kholodkovskaya, V. A. Dolgikh and B. A. Popovkin, *J. Solid State Chem.*, 1994, **112**, 189-191.
82. K. Ueda, S. Inoue, S. Hirose, H. Kawazoe and H. Hosono, *Appl. Phys. Lett.*, 2000, **77**, 2701-2703.
83. S. Inoue, K. Ueda, H. Hosono and N. Hamada, *Phys. Rev. B*, 2001, **64**, 1135-1148.
84. H. Hiramatsu, K. Ueda, H. Ohta, T. Kamiya, M. Hirano and H. Hosono, *Appl. Phys. Lett.*,

- 2005, **87**, 211107.
85. R. Poettgen and D. Johrendt, *Zeitschrift Fur Naturforschung Section B-a Journal of Chemical Sciences*, 2008, **63**, 1135-1148.
86. Y. Kamihara, H. Hiramatsu, M. Hirano, R. Kawamura, H. Yanagi, T. Kamiya and H. Hosono, *J. Am. Chem. Soc.*, 2006, **128**, 10012-10013.
87. T. Watanabe, H. Yanagi, T. Kamiya, Y. Kamihara, H. Hiramatsu, M. Hirano and H. Hosono, *Inorg. Chem.*, 2007, **46**, 7719-7721.
88. Y. Kamihara, T. Watanabe, M. Hirano and H. Hosono, *J. Am. Chem. Soc.*, 2008, **130**, 3296-3297.
89. H. Takahashi, K. Igawa, K. Arii, Y. Kamihara, M. Hirano and H. Hosono, *Nature*, 2008, **453**, 376-378.
90. X. H. Chen, T. Wu, G. Wu, R. H. Liu, H. Chen and D. F. Fang, *Nature*, 2008, **453**, 761-762.
91. C. Wang, L. Li, S. Chi, Z. Zhu, Z. Ren, Y. Li, Y. Wang, X. Lin, Y. Luo, S. Jiang, X. Xu, G. Cao and Z. a. Xu, *EPL*, 2008, **83**.
92. D. Berardan, L. D. Zhao, C. Barreateau and N. Dragoë, *Phys. Status Solidi A*, 2012, **209**, 2273-2276.
93. L. Pinsard-Gaudart, D. Berardan, J. Bobroff and N. Dragoë, *Phys. Status Solidi-RRL*, 2008, **2**, 185-187.
94. S. Arsenijevic, R. Gaal, A. S. Sefat, M. A. McGuire, B. C. Sales, D. Mandrus and L. Forro, *Phys. Rev. B*, 2011, **84**, 075148.
95. H. Hiramatsu, H. Yanagi, T. Kamiya, K. Ueda, M. Hirano and H. Hosono, *Chem. Mater.*, 2008, **20**, 326-334.
96. H. Hiramatsu, H. Kamioka, K. Ueda, M. Hirano and H. Hosono, *J. Ceram. Soc. Jpn.*, 2005, **113**, 10-16.
97. H. Kamioka, H. Hiramatsu, M. Hirano, K. Ueda, T. Kamiya and H. Hosono, *Journal of Luminescence*, 2005, **112**, 66-70.
98. A. P. Richard, J. A. Russell, A. Zakutayev, L. N. Zakharov, D. A. Keszler and J. Tate, *J. Solid State Chem.*, 2012, **187**, 15-19.
99. C. Barreateau, D. Berardan, E. Amzallag, L. D. Zhao and N. Dragoë, *Chem. Mater.*, 2012, **24**, 3168-3178.
100. H. Hiramatsu, Y. Kamihara, H. Yanagi, K. Ueda, T. Kamiya, M. Hirano and H. Hosono, *J. Eur. Ceram. Soc.*, 2009, **29**, 245-253.
101. K. Ueda, H. Hiramatsu, H. Ohta, M. Hirano, T. Kamiya and H. Hosono, *Phys. Rev. B*, 2004, **69**, 155305.
102. H. Ohta, S. Kim, Y. Mune, T. Mizoguchi, K. Nomura, S. Ohta, T. Nomura, Y. Nakanishi, Y. Ikuhara, M. Hirano, H. Hosono and K. Koumoto, *Nat. Mater.*, 2007, **6**, 129-134.
103. R. Kykyneshi, D. H. McIntyre, J. Tate, C. H. Park and D. A. Keszler, *Solid State Sci.*, 2008, **10**, 921-927.
104. H. Hiramatsu, H. Ohta, T. Suzuki, C. Honjo, Y. Ikuhara, K. Ueda, T. Kamiya, M. Hirano and H. Hosono, *Cryst. Growth Des.*, 2004, **4**, 301-307.
105. E. S. Stampler, W. C. Sheets, M. I. Bertoni, W. Prellier, T. O. Mason and K. R. Poeppelmeier, *Inorg. Chem.*, 2008, **47**, 10009-10016.
106. Y.-c. Liu, J.-L. Lan, B. Zhan, J. Ding, Y. Liu, Y.-H. Lin, B. Zhang and C.-w. Nan, *J. Am. Ceram. Soc.*, 2013, **96**, 2710-2713.

107. V. Pele, C. Barreateau, D. Berardan, L. D. Zhao and N. Dragoe, *J. Solid State Chem.*, 2013, **203**, 187-191.
108. S. D. N. Luu and P. Vaqueiro, *J. Mater. Chem. A*, 2013, **1**, 12270-12275.
109. P. Vaqueiro, G. Guelou, M. Stec, E. Guilmeau and A. V. Powell, *J. Mater. Chem. A*, 2013, **1**, 520-523.
110. F. Li, J. F. Li, L. D. Zhao, K. Xiang, Y. Liu, B. P. Zhang, Y. H. Lin, C. W. Nan and H. M. Zhu, *Energy Environ. Sci.*, 2012, **5**, 7188-7195.
111. Y. Liu, L. D. Zhao, Y. C. Liu, J. L. Lan, W. Xu, F. Li, B. P. Zhang, D. Berardan, N. Dragoe, Y. H. Lin, C. W. Nan, J. F. Li and H. M. Zhu, *J. Am. Chem. Soc.*, 2011, **133**, 20112-20115.
112. J.-L. Lan, Y.-C. Liu, B. Zhan, Y.-H. Lin, B. Zhang, X. Yuan, W. Zhang, W. Xu and C. W. Nan, *Adv. Mater.*, 2013, **25**, 5086-5090.
113. J.-L. Lan, B. Zhan, Y.-C. Liu, B. Zheng, Y. Liu, Y.-H. Lin and C.-W. Nan, *Appl. Phys. Lett.*, 2013, **102**, 123905.
114. D. S. Lee, T. H. An, M. Jeong, H. S. Choi, Y. S. Lim, W. S. Seo, C. H. Park, C. Park and H. H. Park, *Appl. Phys. Lett.*, 2013, **103**, 171109.
115. J. Li, J. Sui, Y. L. Pei, X. F. Meng, D. Berardan, N. Dragoe, W. Cai and L. D. Zhao, *J. Mater. Chem. A*, 2014, **2**, 4903-4906.
116. D. R. Clarke, *Surf. Coat. Technol.*, 2003, **163**, 67-74.
117. C. L. Wan, W. Pan, Q. Xu, Y. X. Qin, J. D. Wang, Z. X. Qu and M. H. Fang, *Phys. Rev. B*, 2006, **74**, 144109.
118. C. L. Wan, Z. X. Qu, Y. He, D. Luan and W. Pan, *Phys. Rev. Lett.*, 2008, **101**, 085901.
119. J. Y. Cho, X. Shi, J. R. Salvador, G. P. Meisner, J. Yang, H. Wang, A. A. Wereszczak, X. Zhou and C. Uher, *Phys. Rev. B*, 2011, **84**, 085207.
120. D. S. Sanditov and V. N. Belomestnykh, *Techn. Phys.*, 2011, **56**, 1619-1623.
121. M. Roufosse and P. G. Klemens, *Phys. Rev. B*, 1973, **7**, 5379-5386.
122. E. J. Skoug, J. D. Cain and D. T. Morelli, *Appl. Phys. Lett.*, 2011, **98**, 261911-261913.
123. B. L. Huang and M. Kaviani, *J. Appl. Phys.*, 2006, **100**, 123507.
124. R. Venkatasubramanian, E. Siivola, T. Colpitts and B. O'Quinn, *Nature*, 2001, **413**, 597-602.
125. C. Barreateau, D. Berardan, L. D. Zhao and N. Dragoe, *J. Mater. Chem. A*, 2013, **1**, 2921-2926.
126. L. D. Zhao, B. P. Zhang, J. F. Li, H. L. Zhang and W. S. Liu, *Solid State Sci.*, 2008, **10**, 651-658.
127. J. J. Shen, L. P. Hu, T. J. Zhu and X. B. Zhao, *Appl. Phys. Lett.*, 2011, **99**, 124102.
128. J. Li, J. Sui, Y. Pei, X. Meng, D. Berardan, N. Dragoe, W. Cai and L.-D. Zhao, *J. Mater. Chem. A*, 2014, **2**, 4903-4906.
129. T. Ohtani, Y. Tachibana and Y. Fujii, *J. Alloys Compd.*, 1997, **262**, 175-179.
130. W. Xu, Y. Liu, L. D. Zhao, P. F. An, Y. H. Lin, A. Marcelli and Z. Y. Wu, *J. Mater. Chem. A*, 2013, **1**, 12154-12158.
131. J. Horak, Z. Stary, P. Lostak and J. Pancir, *J. Phys. Chem. Solids*, 1990, **51**, 1353-1360.
132. L. Pan, D. Berardan, L. D. Zhao, C. Barreateau and N. Dragoe, *Appl. Phys. Lett.*, 2013, **102**, 023902.
133. D. F. Zou, S. H. Xie, Y. Y. Liu, J. G. Lin and J. Y. Li, *J. Mater. Chem. A*, 2013, **1**, 8888-8896.